

High-Speed

8. High-Speed Electron Microscopy

Geoffrey H. Campbell, Joseph T. McKeown , Melissa K. Santala 

High-speed electron microscopy has emerged as a well-established in situ transmission electron microscopy (TEM) capability that can provide observations and measurements of complex, transient materials phenomena with high spatial and temporal resolutions. The development and advancement of the two categories of high-speed electron microscopy, each optimized for specific regimes of spatial and temporal resolutions—single-shot dynamic TEM (DTEM) and stroboscopic or ultrafast TEM (UTEM)—are reviewed and the technologies employed in both techniques are described. Limitations of the techniques are described and example applications are provided. Finally, an outlook for future development of time-resolved electron microscopy is provided, offering potential directions for new levels of performance and flexibility.

8.1 Technologies of High-Speed Electron Microscopy	456
8.1.1 Anatomy of a High-Speed Electron Microscope.....	456
8.1.2 Photoelectron Guns.....	459
8.1.3 Materials for Photoelectron Guns.....	460
8.1.4 Lasers.....	461
8.2 Limitations	462
8.2.1 DTEM Limitations.....	462
8.2.2 UTEM Limitations.....	469
8.3 Applications of High-Speed Electron Microscopy	470
8.3.1 DTEM Applications.....	471
8.3.2 UTEM Applications.....	471
8.4 Outlook	476
8.4.1 Improving and Bridging Temporal Resolutions.....	476
8.4.2 Further Directions for High-Speed Electron Microscopy.....	477
8.5 Conclusions	478
References	478

Throughout its history, transmission electron microscopy (TEM) has been performed on static samples, with images recorded on film using exposure times of a few seconds. Yet the first in situ experiments in the transmission electron microscope were performed shortly after its routine deployment as a tool to investigate microstructure in thin metal films [8.1, 2], and actual observations of moving dislocations were reported in 1956 [8.3], illustrating the interest in materials dynamics that has existed from the early days of implementation of the TEM.

Many phenomena in physics, chemistry, biology, and materials science require understanding the dynamics of processes across length and timescales that span orders of magnitude (i. e., pico-, nano-, micro-, mesoscales). Experimental techniques developed to probe these regimes in space and time include free-electron x-ray lasers, short (femtosecond) laser pulses, optical techniques, and ultrafast electron diffraction

(UED), the last of which has been developed with temporal resolutions approaching that of the optical and x-ray methods [8.4–11]. Although all of these methods are powerful, the widespread use of and accompanying extensive literature demonstrate that there are significant benefits to the high-spatial-resolution imaging capability of TEMs, which often provides a more direct interpretation of structure and its evolution. The ever-expanding role of in situ TEM as a characterization tool further demonstrates the need to identify through imaging the transient states of processes, which are often far more important than just the starting and ending states, particularly for the development and validation of predictive modeling capabilities.

In situ TEM has been constrained by conventional video frame rates (30 Hz or \approx 33 ms), though recent advances in cameras based on CMOS (complementary metal-oxide semiconductor) and direct detection cameras have reduced these frame rates to 300 Hz (\approx 3 ms)

Table 8.1 Overview comparison of UTEM and DTEM

	Stroboscopic/ultrafast TEM (UTEM)	Single-shot/dynamic TEM (DTEM)
# Electrons/pulse	$\approx 1-10$	$\approx 10^7-10^{10}$
# Pulses/image	$\geq 10^5$	1
Temporal resolution	fs	ns
Spatial resolution	Å	$\approx 10-20$ nm
Strength	Spatiotemporal resolution	Image irreversible processes in real space
Weakness	Reversible processes only	Resolution

and even 1600 Hz ($\approx 625 \mu\text{s}$), respectively, using sub-area sampling rates [8.12]. However, many dynamic processes require temporal resolutions of nanoseconds and higher, and gaining an understanding of these rapidly evolving physical phenomena has motivated the development of high-speed electron microscopy.

High-speed TEM can be separated into two categories, each optimized for specific regimes of spatial and temporal resolutions: stroboscopic or ultrafast TEM (UTEM) and single-shot or dynamic TEM (DTEM). These techniques are summarized in Table 8.1, in which it is evident that high-speed TEM occupies a parameter space that lies between x-ray free-electron lasers (XFELs) and MeV electron beam diffraction methods in terms of spatial and temporal resolutions [8.13–15]. In both high-speed TEM cases, electron pulses are generated by laser-induced photoemission, with modifications to the TEM column to allow lasers to access the electron gun and the specimen. The stroboscopic ap-

proach achieves atomic-level spatial resolution and sub-picosecond time resolution using femtosecond lasers to accrue signals from millions of identical pump–probe experiments [8.16–20]. This requires highly repeatable, reversible processes, such as electronic excitations and elastic deformation. The single-shot approach attains nanometer and nanosecond resolutions in space and time using single intense electron pulses [8.21–30], and this technique is suited to the study of unique, irreversible processes, such as microstructure evolution and phase transformations [8.31–38]. While both approaches have been advanced significantly over the past decade or so, the history of both techniques dates back many decades. In this chapter, we review the development and advancement of high-speed electron microscopy, describing the technologies employed in UTEM and DTEM. We discuss the performance, limitations, and applications and conclude with a look to the future of these instruments.

8.1 Technologies of High-Speed Electron Microscopy

8.1.1 Anatomy of a High-Speed Electron Microscope

Two approaches exist for time-resolved electron microscopy: single-shot [8.21] and stroboscopic [8.17]. In the single-shot approach, a single pulse of electrons is used to capture the image or diffraction pattern of the specimen. This approach requires upwards of several 10^9 electrons in the single pulse. The highest time resolution of this approach is limited to the nanosecond regime due to space-charge effects that will be discussed elsewhere in the chapter. It is appropriate for capturing irreversible processes in materials such as phase transformations, plastic deformation, or any microstructure evolution. The other approach, stroboscopic or pump–probe, is done with millions or billions of pulses, each containing one to several electrons. The specimen is repeatedly pumped into a specific state and then probed at a distinct and highly time-resolved point in time after the pump event. The reduced charge in each pulse compared to the single-shot approach means

that space charge is not an issue and the time resolution is pushed into the femtosecond regime. This approach is appropriate for studying physical phenomena that are highly repeatable, such as electronic transitions and elastic vibrations.

Both approaches are implemented on a transmission electron microscope platform. The platform is augmented by integration with one or more lasers that allow it to be operated in a pulsed mode. The base microscope is a commercially available instrument, but the lasers have typically been interfaced to the microscope by modifications performed in the investigators laboratories. Only recently has a commercial venture been offering this integration capability.

Single-Shot (DTEM)

The single-shot approach was first pioneered at the Technische Universität (TU) Berlin [8.39–41] and then extended at Lawrence Livermore National Laboratory (LLNL) [8.29]. The layouts of the systems share much in common (Fig. 8.1). The central element is a TEM

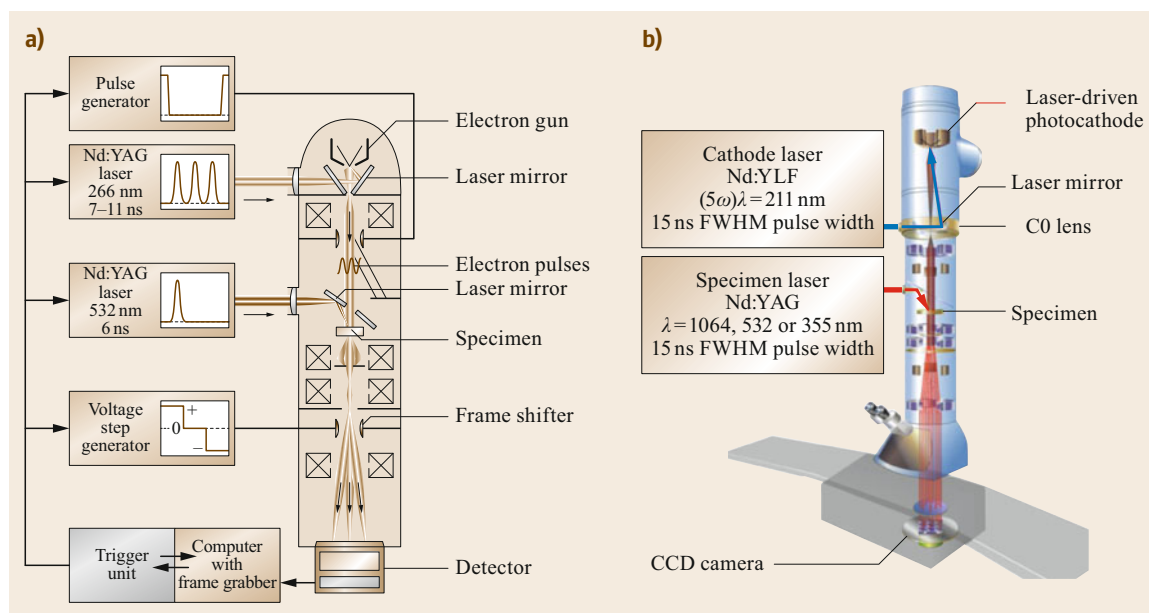


Fig. 8.1a,b Schematic comparison of (a) TU Berlin DTEM and (b) LLNL single-shot DTEM. Reprinted from [8.24], with permission from Elsevier

that is interfaced to laser systems. The cathode laser generates a pulse of ultraviolet (UV) light with a photon energy greater than the work function of the material used as the photocathode. The light pulse is introduced to the vacuum column of the microscope through an appropriate window, typically fused silica, which can transmit the frequency without appreciable losses. Optical elements within the vacuum system direct the laser pulse to the electron gun and onto the photocathode [8.27].

The electron gun used to date for single-shot DTEM has been a conventional thermionic system, originally developed for tungsten hairpin or LaB₆ crystal emitters that are heated to high temperature. Moreover, the photocathodes have been built onto the tip of a refractory metal wire hairpin. This arrangement offers the advantage of being able to heat the hairpin to achieve thermionic emission of electrons and thus operate the microscope in continuous wave (CW) mode for alignment and experimental setup. For pulsed mode, the current to the cathode is turned off and the laser pulse generates all of the electrons by photoemission. The ability to operate the same cathode in both the pulsed and CW modes offers significant operational advantages, as well as the ability to acquire CW images to assist with unambiguous interpretation of pulsed images.

The electrons that are emitted from the surface of the cathode by photoemission are drawn away from the surface by the electrostatic field generated by the electron accelerator. According to Child's Law [8.42], the

current drawn out from a cathode surface depends on the applied field strength. The field generated by the accelerator has a fairly weak gradient, and this had led to speculation that increased current could be achieved in electron guns that apply high fields to the cathode, such as in a field-emission-type electron gun. However, this approach has not yet been implemented and it is not clear that the same emitter could support both CW and pulsed modes in such an arrangement.

Once the electrons are emitted by the gun assembly, they enter the acceleration gun of the microscope and are accelerated up to an energy of, typically, 200 keV. The illumination section of the microscope is the first place that the electrons encounter electron-optical elements that act to focus them. The DTEM has an additional, weak condenser lens, called the C0 lens, placed before the condenser lenses of the original microscope design. The purpose of this first lens is to steer the beam through the microscope section containing the mirror that reflects the cathode laser pulses up the column to the gun without clipping on any of the optical elements [8.27]. This lens has the added benefit that it efficiently couples all of the electrons emitted at the gun into the microscope column, maximizing the brightness of the illumination.

The electron pulse travels down the column of the microscope in the same way as would a CW beam. The optical elements of the microscope act on the electrons and are able to control the characteristics of the electron illumination on the specimen and subsequent image or

diffraction pattern formation. The main difference between pulsed and CW operation of the microscope is a degradation of the image resolution due to the space-charge effects. However, the pulsed electrons retain sufficient coherence to form dynamical diffraction features in the image. All of the crystal defects that control material properties, such as precipitates, dislocations, stacking faults, twins, and grain boundaries, can be imaged with the commonly interpretable contrast features that are expected from dynamical contrast in the TEM. This is achieved by using an objective aperture to produce contrast, as in conventional diffraction-contrast imaging in a TEM. This also serves to decrease the number of electrons in the beam as it passes through the projector lens system, where the numerous crossovers can produce image distortions if space-charge effects are significant. It should be noted that many of the fixed apertures, particularly between the electron gun and the first condenser lens, have been removed from the DTEM to maximize the number of electrons directed to the specimen for imaging.

The final element of the DTEM is the camera. The cameras used by DTEM are the same as those used for standard TEM. No time-resolution requirements are imposed on the camera because those parameters are all determined by the characteristics of the electron pulse generated in the gun. The camera is composed of a scintillator that converts the incident energetic electrons to light signals that are coupled to a CCD detector by, typically, a fiber-optic bundle. Since the number of electrons in a pulse is limited, it is desirable to detect all of the electrons in the camera, and single-electron-sensitive sensors are now standard in currently available electron microscope cameras.

Movie-Mode Single-Shot (DTEM)

The instrument described above is capable of acquiring one time-resolved image at a specific time after a specimen pump laser pulse arrives at the specimen. The limitations on measuring kinetics with just a single image became obvious, and the capability to acquire multiple images of a single event as it unfolds with time was built [8.28, 33]. Similar capabilities have been developed previously [8.41, 43, 44], but this new capability requires that a train of electron pulses be created at the photocathode. A new type of cathode laser is required that can generate an arbitrary waveform (and will be described in more detail in Sect. 8.1.4).

This laser can generate a pulse duration that is user-defined, from a minimum of 15 ns to a maximum of $> 1 \mu\text{s}$. It can also generate a user-defined number of pulses, which is usually set to nine pulses for reasons that will become clear shortly. These pulses may be arbitrarily spaced in time, within the overall envelope of

the laser capabilities determined by the energy content and decay time of the laser amplification medium.

The next component of this capability is fast electrostatic deflection plates that are located low in the column. The two sets of plates are oriented orthogonally, such that they can deflect the (typically) nine electron pulses into an array of three by three nonoverlapping images on the square CCD detector. A schematic of the LLNL movie-mode DTEM is shown in Fig. 8.2.

Stroboscopic (UTEM)

The idea for periodically illuminating a microscope specimen with an electronically deflected electron beam while simultaneously pumping the specimen at the same frequency was first proposed and demonstrated in the 1960s [8.46]. It was subsequently modified to use photoemission with pulsed lasers in the 1980s [8.43, 47], and it was finally incorporated into modern high-resolution instrumentation recently, where femtosecond time resolution was demonstrated [8.16, 19]. A schematic of the UTEM developed at the California Institute of Technology (Caltech) [8.16] is shown in Fig 8.3.

The instrumentation for stroboscopic microscopy shares a superficial resemblance to single-shot, but there are significant differences, especially in the laser systems employed. Significantly, a femtosecond pulsed laser with a high repetition rate in the MHz regime is typically used. This family of lasers is usually based on Ti-doped sapphire that lases at 800 nm. These systems will typically have pulse durations of 100 fs or less and it will be the only laser, as opposed to two separate lasers on the single-shot instruments. The fs laser pulses are split with a beam splitter, and one leg is sent to the specimen while the other leg is sent through a time delay arrangement and on to the photocathode. The relative arrival times of the split laser pulse legs is controlled through adjusting the path length of one leg versus the other.

The part of the fs pulse of light that is sent to the photocathode is frequency converted to third harmonic (267 nm), sent through the adjustable delay line, introduced into the vacuum of the microscope column, and brought to the electron gun. The pulse creates a small number of photoelectrons at the photocathode, of which approximately one electron per pulse is actually accelerated and injected into the electron-optical column of the microscope. The issue of space charge is thus obviated.

The other branch of the pulse is brought to the specimen in the microscope and used to pump a response in the specimen. The delay line on the photocathode branch is adjusted such that the arrival time of the single electron traveling down the column arrives at the spec-

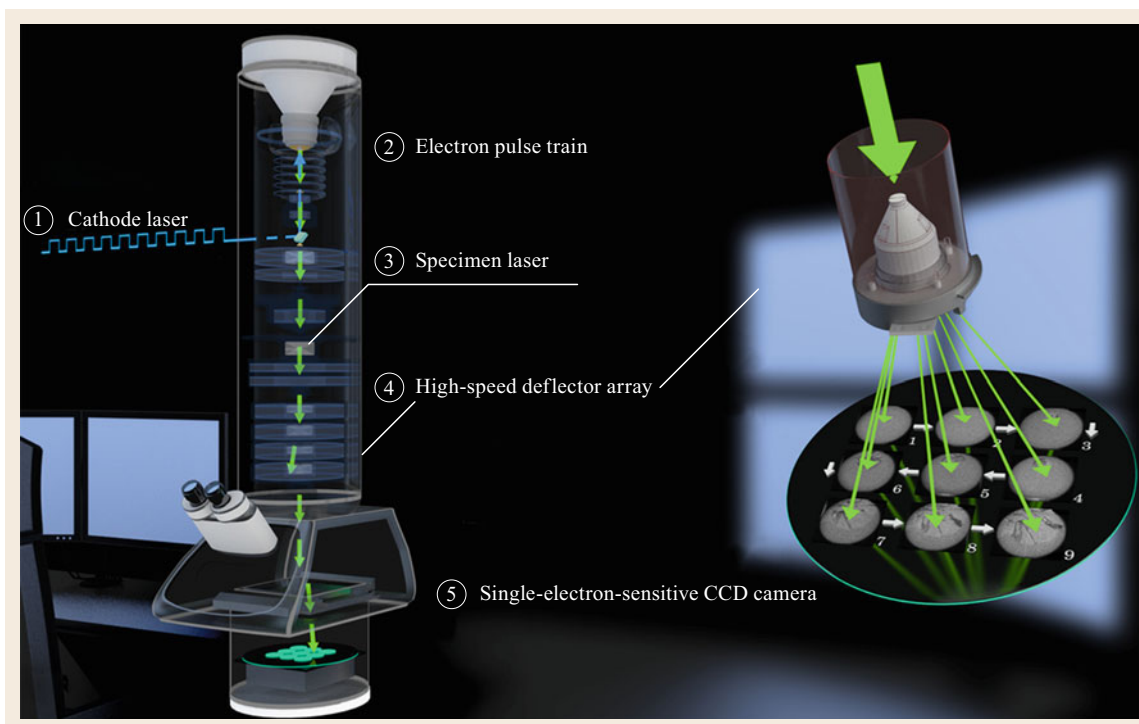


Fig. 8.2 Schematic of movie-mode DTEM, illustrating (1) the arbitrary waveform generation (AWG) cathode laser producing a train of UV pulses to generate (2) electron pulses with the same temporal pattern. (3) The specimen laser initiates the process to be studied, and (4) a high-speed deflector array (shown in detail on the right-hand side of the image) rapidly switches each pulse to a different region of (5) a single-electron-sensitive CCD camera. Figure created by Ryan Chen of the Technical Information Department (TID) at Lawrence Livermore National Laboratory

imen position at a specific time relative to the pump pulse. If the desired image requires, for example, 10^9 electrons to achieve a particular signal-to-noise ratio, then this pump-probe cycle must be repeated $\approx 10^9$ times. To map out the time evolution of the process, the delay between pulses is changed by altering the delay line path length and repeating the image acquisition. A fundamental consideration for the experiment is that it unfolds in exactly the same way for the billions of image acquisitions. This consideration makes the technique suited to only those processes that are reversible, such as elastic vibrations [8.48, 49] and electronic transitions [8.50].

8.1.2 Photoelectron Guns

To date, the electron guns that have been used as photoelectron guns have been essentially the same guns made by the electron microscope manufacturers for CW emission. These have been the thermal-emission type of gun that uses either a hot filament of W or a heated crystal of a low work function material, such as LaB₆, as the electron source in CW mode. These filament materials

have then been used also for the pulsed source, with some modifications discussed below. The electrons generated at the cathode source are drawn away from the surface by the accelerating potential of the microscope. The negative bias applied by the Wehnelt assembly acts to focus the electrons to their first crossover.

An important consideration for the electron gun is the constraint imposed by Child's Law [8.42]. This relation reveals the important role of the gun and the characteristics of the laser pulse in optimizing the charge extracted during time-resolved operation of the microscope. In particular, the higher the field gradient at the photocathode surface the more charge that can be extracted. However, the gradient is set by the accelerating potential of the microscope, and it is comparatively shallow because it has been designed for minimum ripple during CW operation to minimize energy spread in the electron beam. Higher gradients are present in field-emission guns (FEGs), but they offer the complication of needing a sharp tip for field emission, which does not offer a good target for a laser pulse. Thus, no field-emission sources have yet been tried for time-resolved operation. The other factor introduced by consideration

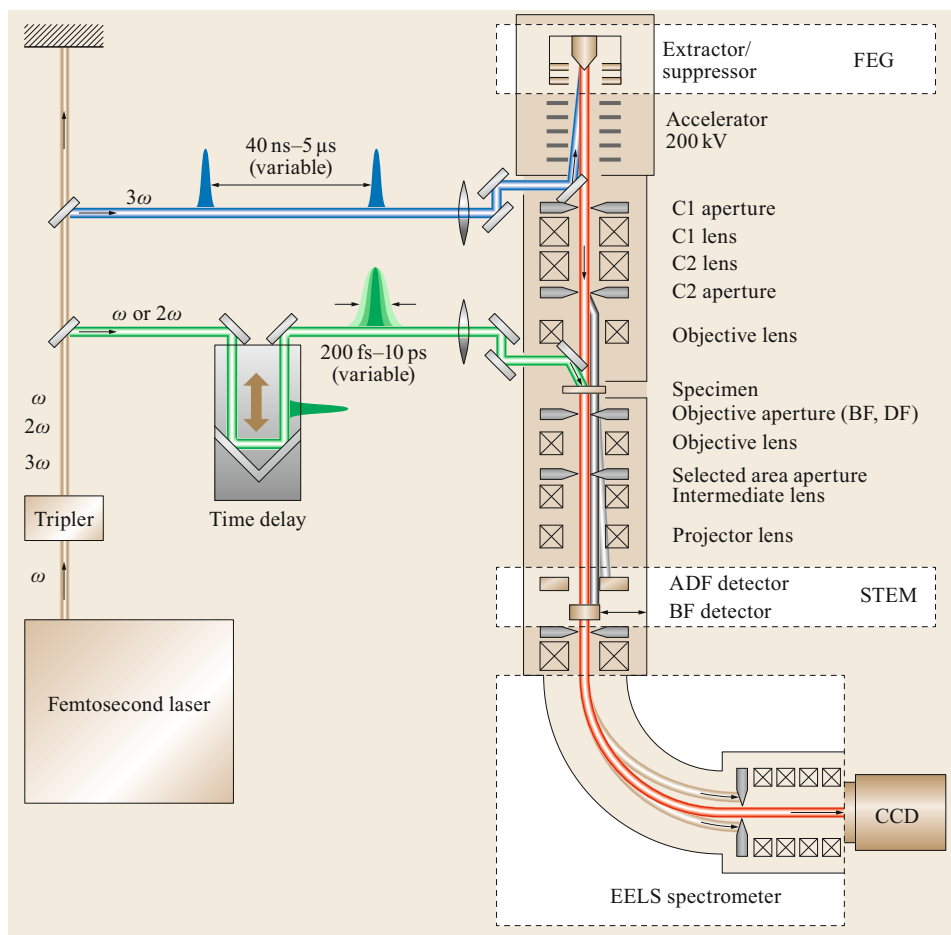


Fig. 8.3 Schematic of the Caltech UTEM, showing the optical, electric, and magnetic components. The optical pulse train generated from the laser, with a variable pulse width of 200 fs–10 ps and a variable repetition rate of 200 kHz–25 MHz, is divided into two parts after harmonic generation. The frequency-tripled optical pulses are converted to the corresponding electron probe pulses at the photocathode in the hybrid FEG. The optical pump branch of the laser excites the specimen with a well-defined time delay with respect to the electron probe pulse. The electron probe pulses can be recorded as an image (conventional TEM image or filtered, EFTEM), a diffraction pattern, or an electron energy-loss spectrum. The STEM bright-field detector is retractable when not in use. Reprinted (adapted) with permission from [8.45]. Copyright 2007 American Chemical Society

of Child's Law is the need to reduce spatial and temporal structure in the laser fluence. Even illumination, with no hot spots or temporal spikes, will produce the greatest charge emitted from the photocathode surface because of the tendency of the emitted charge to saturate as fluence increases.

8.1.3 Materials for Photoelectron Guns

The goal of material choice for the photocathode is to optimize the efficiency of electron emission. The typ-

ical considerations are the work function and physical robustness. The work function of the material should be chosen based on the photon energy of the cathode laser. Single photon absorption is much more efficient than multiphoton absorption for emission. Likewise, the greater the spread between the work function and photon energy allows residual kinetic energy to improve the efficiency of the electrons actually escaping from the surface. The physical robustness of the material comes into play because of the repeated laser illumination that can cause thermal cycling or material ablation.

Semiconducting Emitters

The early development of single-pulse microscopy invested much effort in the development of materials for the photocathode, with emphasis on semiconducting materials [8.40]. One of the best materials found after these investigations was ZrC, because of its combination of low work function and refractory properties. Moreover, it was found to work best with a rough surface, where the jagged irregularities would create field enhancements near the surface for greater efficiency in extracting the charge. These emitters were formed by electrophoresis of ZrC powder onto the tip of a standard W hairpin emitter. Heating of the hairpin by direct current in a vacuum allowed the adhered powder to sinter and create a structure somewhat robust to laser illumination, but these emitters did suffer from limited lifetime.

Stroboscopic microscopy has generally less stringent requirements on the photocathode due to the lower energy delivery from the low duty cycle of the laser. These photocathodes have typically been based on the standard LaB₆ single crystals that are used for thermal emission in electron microscopes.

Metallic Emitters

The recent development of single-shot microscopy with the DTEM at LLNL has used Ta as the photocathode material. Ta metal is structurally robust because it is a ductile metal, and its high melting point also makes it robust to material ablation. While its work function is somewhat higher than semiconductor materials, the use of fifth harmonic (211 nm) photons makes the photoemission process efficient. The form of the emitter is a simple disk of Ta with 800 μm diameter that has been welded to the tip of a wire hairpin emitter, as shown in Fig. 8.4. The simplicity and long life of this emitter has made it the preferred choice.

8.1.4 Lasers

The requirement of single-shot time-resolved microscopy to generate all of the electrons needed for the image in a single pulse generally dictates that substantial laser energy is used for photoemission. The experience with the DTEM at LLNL is that the fifth harmonic of an Nd:YLF laser (fundamental 1053 nm) works well for efficient generation of photoelectrons from a Ta metal photocathode. Using the fifth harmonic, with the associated losses in energy during the frequency conversion, means that a pulse energy around 100 mJ in the fundamental is required. Moreover, precise control of the spatial and temporal pulse shaping is needed.

The spatial profile that maximizes the electron emission from the photocathode is a *top hat* profile. That is to say, the intensity of the photon fluence is constant across the diameter of the circular illumination spot on the cathode. Fine-scale structure such as hot spots should be avoided. This profile is achieved through relay imaging a filled aperture to the position of the photocathode.

The temporal profile of the laser pulse energy should also be flat topped, which helps to avoid the effective brightness degradation from time-varying space-charge effects [8.30]. Moreover, the duration of the pulse should be adjustable to the requirements of the experiment. The longer the pulse, the more charge can be extracted from the photocathode. Thus, for experiments that require lower time resolution the pulse can be lengthened and better signal-to-noise ratio can be achieved in the image. These characteristics of the laser pulse have been accomplished in the LLNL DTEM with an arbitrary waveform generator to create seed pulses for the amplification system. The seed pulse counters the system's natural tendency to create a Gaus-

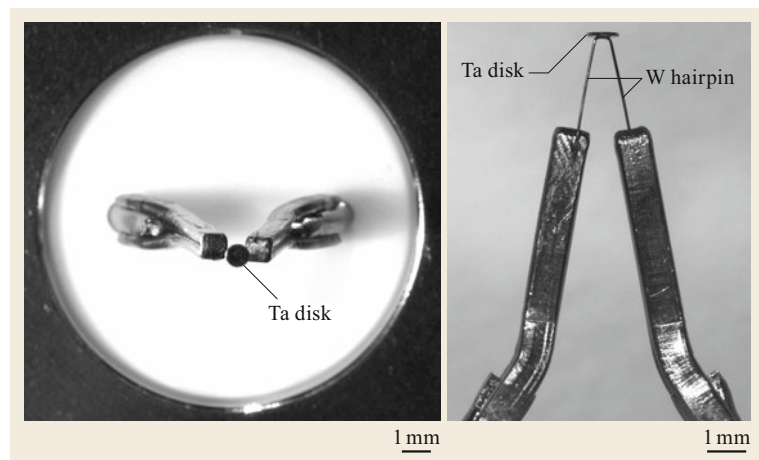


Fig. 8.4 Photographs of an 800- μm Ta disk that has been welded to the tip of a wire hairpin emitter, used as the photocathode in the LLNL DTEM

sian waveform and instead forces it to make a pulse of constant intensity for the entire pulse duration.

The arbitrary waveform generator also enables a new mode of operation for the instrument called movie mode, in which multiple images are recorded of a specimen during a single experiment as its structure evolves. The arbitrary waveform generator creates a train of pulses, separated by user-defined time intervals, which is introduced into the amplification and frequency conversion systems. The laser pulse train cre-

ates a series of electron pulses at the photocathode that are introduced to the microscope column. To record the image in each pulse, fast deflection plates are placed in the lower part of the column, directly above the viewing chamber. These electrostatic plates steer each pulse to a different patch of the phosphor screen that is optically coupled to the CCD image-recording device. In this way, nine images are typically recorded in a 3×3 array tracking the time evolution of the specimen during the experiment.

8.2 Limitations

Both DTEM and UTEM are photoemission techniques with high temporal resolution, but they differ greatly in their capabilities, strengths, and limitations. DTEM is distinguished from UTEM in that each photoemitted pulse contains enough electrons to form an image or diffraction pattern. While this makes DTEM suitable for imaging irreversible reactions, limitations arise in the spatial and temporal resolution due to the extremely high instantaneous electron current density. The high current density can also result in different damage mechanisms.

In UTEM, the electron emission is precisely controlled by the incidence of the laser on the cathode, but neither the total electron dose nor the current density need be higher than in conventional TEM. Thus, the limitations in spatial resolution due to high current density do not apply to UTEM, but there are other limitations to spatial resolution as well as to the specimen and types of reactions that can be probed. Damage due to exposure to the photoemitted pulses in UTEM is not expected to exceed those of conventional TEM imaging, but damage may accrue from repeated excitation of the sample.

8.2.1 DTEM Limitations

DTEM Temporal Resolution

The major consideration for temporal resolution in DTEM is the resolution required for acquisition of a single image or diffraction pattern. Thus, the temporal resolution of the DTEM in imaging or diffraction is determined by the duration of the electron pulse at the sample. Depending on the application, $\approx 10^6$ – 10^8 electrons are needed at the detector to form an image with sufficient signal-to-noise ratio to be useful [8.22, 27]. More electrons must therefore be generated at the source, as some will be scattered to high angles or purposely excluded by apertures (e. g., to increase contrast), and therefore each pulse requires $\approx 10^9$ – 10^{10}

electrons at the photocathode in order to form an image that is not limited by noise.

To date, DTEM has been realized with electron pulses that deliver the required number of electrons over several nanoseconds. In this regime, the electron pulse length is essentially equal to the cathode laser pulse length, as the mechanisms that degrade the time resolution relative to the cathode laser pulse duration typically occur on the picosecond scale. An electron pulse from a photocathode will undergo temporal broadening during propagation due to an initial energy distribution in the pulse, trajectory differences in the drift region, and space-charge effects [8.51].

Temporal expansion due to the energy spread in the electron pulse in the initial acceleration region is of order

$$\Delta t_E = \frac{(2m\Delta E)^{\frac{1}{2}} d}{eV_0}, \quad (8.1)$$

where m and e are the electron mass and charge, ΔE the energy spread, d the cathode–anode distance, and V_0 the accelerating voltage [8.51–53]. This contributes a few picoseconds or less to the temporal broadening for typical DTEM parameters. The temporal spread due to space-charge effects in the initial acceleration region is

$$\Delta t_{SC}^{\text{accel}} = \frac{\left(\frac{em}{2}\right)^{\frac{1}{2}} d^2 N}{\pi V_0^{\frac{3}{2}} \epsilon_0 r_b^2}, \quad (8.2)$$

where N is the number of electrons in the pulse, ϵ_0 is the vacuum permittivity, and r_b is the radius of the electron beam [8.51]. In the drift region, the temporal spread due to space-charge effects is

$$\Delta t_{SC}^{\text{drift}} = \frac{\left(\frac{em}{2}\right)^{\frac{1}{2}} L^2 N}{4\pi V_0^{\frac{3}{2}} \epsilon_0 r_b^2}, \quad (8.3)$$

where L is the length of the drift region [8.51]. From (8.2) and (8.3), it can be seen that small d and L and large V_0 and r_b are favorable to reduce space-charge effects. For current DTEM parameters, the temporal spread of the electron pulse is expected to be less than a nanosecond. The electron pulse is much longer than it is wide—a 20-ns, 200-keV pulse will be ≈ 300 cm in length but a fraction of a millimeter in diameter (depending on lens settings and position within the column). In this high-aspect-ratio limit, longitudinal space-charge effects can be practically neglected except near the leading and trailing edges of the pulse.

The DTEM at LLNL has been operated with individual photoemitted electron pulses ranging from 1.5 ns for single-shot electron diffraction [8.31] to 15–50 ns for electron imaging experiments [8.24, 38]. For a DTEM functioning in the nanosecond regime, the time resolution will be controlled essentially by the photocathode pulse length. Pushing the single-frame temporal resolution to shorter timescales (i. e., 1 ns or below) will be challenging but may be possible through the use of relativistic beams. Simulations have demonstrated the feasibility of generating an electron pulse in the picosecond range with adequate intensity for single-shot DTEM [8.54, 55]. However, considerable challenges remain in the design of electron optics for imaging with relativistic electron pulses. Beam damage may also be a limiting factor [8.25].

DTEM is signal-limited even in the nanosecond regime, such that the optimal time resolution is dictated by the required fluence at the sample, the brightness of the electron source, and the maximum tolerable convergence angle. Even if an adequate number of electrons can be emitted, the limiting factor to the temporal resolution will be space-charge effects, which will degrade spatial resolution even with an optimized source and column design. Brightness and the factors limiting spatial resolution are considered in Sect. 8.2.1 *DTEM Spatial Resolution*.

While the time resolution for a single electron pulse is dictated by the required total electron fluence at the sample and directly controlled by the photocathode laser pulse duration, the interframe time resolution in a multiframe experiment is controlled by (1) the ability to produce a series of uniform electron pulses with adequate intensity and a desired interframe spacing and (2) the ability to detect and store the rapidly generated electron images. At LLNL, the pulsed cathode laser system is operated at 10 Hz. To produce a pulse train with nano- to microsecond spacing between pulses, the AWG laser is used to temporally shape each of the laser pulses produced at 10 Hz. The AWG uses a waveform generator to drive a fiber-based electro-optical modulator that temporally shapes a continuous fiber laser seed

pulse, essentially carving out a series of shorter, closely spaced pulses from the longer pulse to allow easy modifications to both the pulse duration and interframe spacing. The modulated waveforms are then amplified to energies of ≈ 1 J using free-space diode laser heads. An upper limit of $\approx 100 \mu\text{s}$ on the total length of the pulse train arises from the temporary depletion of the lasing media in the amplification stages [8.28, 30].

Cameras with single-electron sensitivity, high-dynamic-range and nanosecond readout times are still well beyond current detector technology. This limitation was overcome in the LLNL DTEM using a custom-built, high-speed electrostatic deflector array installed between the sample and the CCD camera to direct each electron pulse in the pulse train to a different region of the camera. The entire image sequence is read out as a single CCD exposure at the end of the experiment and segmented into separate frames. Typically, 9-frame movies are generated, though it is possible to produce 16 or 25 frames with the AWG and deflector system, though this has not been done because of the loss of spatial resolution that would accompany the implementation of a higher number of frames with the current $2k \times 2k$ CCD camera used with the DTEM. The electrostatic deflector system places a lower limit on the temporal spacing between two sequential pulses in a pulse train, because of residual blur as the voltage in the deflectors settles to its final value (limited by the slew rate of the high-voltage electronics) [8.24]. Currently, the interframe spacing in the LLNL DTEM is limited to 50 ns, and start-to-start interframe times of 70 ns (using a 20-ns electron pulse) have been achieved [8.56].

Developments in high-speed camera technologies [8.57] that use on-chip buffered storage to achieve high frame rates [8.58–61] have the potential to dramatically increase the maximum number of frames that can be captured, especially if they are developed along with a timed electrostatic frame shifter. The gains that have been seen in optical photography would have to be adapted for electron detection [8.24]. Any increase in the number of frames requires a matching rapid repetition in production of the required cathode laser pulses. Advances in camera and laser systems would enable DTEM movie acquisitions with dozens or hundreds of frames [8.28]. Experiments of this kind would entail collecting, handling, storing, and analyzing large data sets, though this issue is not unique to high-speed TEM.

Finally, the temporal resolution with respect to the timing between the specimen trigger and the electron probe pulse may be accurate to within ≈ 100 fs if both are generated from the same beam-split laser pulse [8.11]. However, the typical time delays required for DTEM experiments are on the nanosecond to microsecond timescales, and it is impractical to implement

these time delays with an optical delay line. For this reason, separate lasers are used to trigger the reaction in the specimen and induce photoemission in the DTEM at LLNL. In this case, the uncertainty in the delay depends on the jitter in the timing system, which is ≈ 1 ns [8.24]. When a trigger other than a laser is used, such as heating from an in situ nanocalorimeter [8.62] or a piezo-driven in situ straining holder [8.63, 64], the uncertainty in the delay may be longer than 1 ns, depending on the response time of the triggering device.

It is instructive to compare the time resolution in DTEM with that of conventional in situ TEM. Conventional in situ TEM is typically limited to video rate imaging (≈ 30 ms per frame), though newer commercially available cameras can achieve faster imaging (≈ 3 ms per frame) but with limitations on the number of electrons reaching the detector. Considering the current limitations of multiframe DTEM acquisitions—the minimum interframe spacing (≈ 50 ns per frame), the maximum number of frames that fit into a single CCD readout, and the upper limit on the duration of a single pulse train (≈ 100 μ s)—a gap of several orders of magnitude still exists between the frame rates achievable with conventional in situ TEM and DTEM. Thus, materials processes that evolve over hundreds of microseconds to milliseconds are too slow for DTEM and too fast for conventional in situ TEM. Bridging this temporal gap remains a significant and costly engineering challenge, which will likely involve DTEM (to address the brightness requirements of short pulses) and fast detector technology [8.30, 65].

DTEM Spatial Resolution

The ability of a conventional static TEM to attain sub-angstrom resolution depends on factors such as beam brightness, energy spread, lens aberrations, and sample quality. All of these are typically compromised in

the DTEM. The peak current during a pulsed exposure in the DTEM is in the low milliamp range, orders of magnitude higher than the nanoamp operation regime of a conventional TEM [8.22]. If the sample can survive this high required fluence, the instrument's resolution limit lies in the electron optics and electron–electron interactions, including space-charge effects, stochastic blurring, and Boersch effects [8.66–68]. These effects can be substantial in the DTEM, because of its extremely high electron current densities relative to conventional static TEM.

Coulombic repulsion between electrons degrades DTEM spatial resolution through redistributions within an electron pulse that manifest as space-charge effects and stochastic blurring. Space-charge effects result in a global expansion of the electron pulse, which may be considered as a negative lens to first order, provided the illumination is uniform [8.22]. This effect could be compensated for with standard TEM electron optics, but in reality, the electron distribution is nonuniform, and higher orders cause aberrations in the space-charge lensing. Global space-charge effects may therefore change both the effective focal lengths and aberration coefficients of each of the lenses. Space-charge defocusing would merely require a readjustment of the lens currents and a possible recalibration of the microscope in pulsed mode, though the effects of space-charge-induced spherical aberration will remain and degrade the resolution. For the DTEM at LLNL, the optimum objective lens currents for conventional thermionic and pulsed imaging modes are close, allowing for fine adjustments to the defocus in pulsed mode.

Stochastic blurring, or the trajectory displacement effect [8.67, 68], results in an irretrievable loss of image information in an electron beam or pulse due to random electron–electron scattering events. This is shown

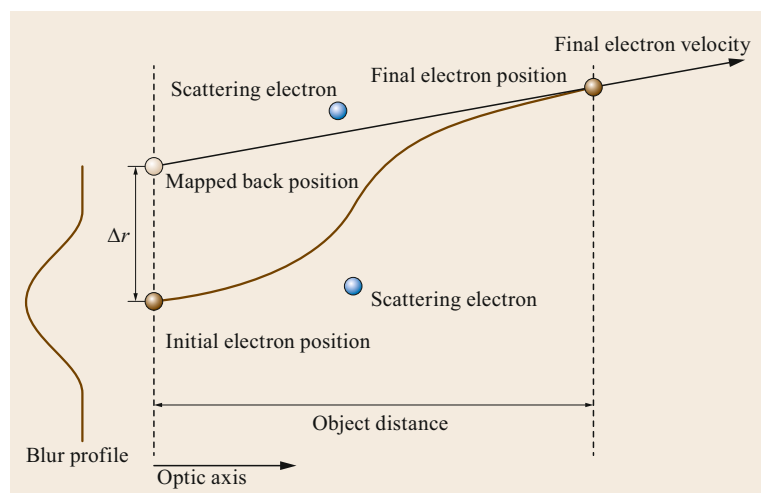


Fig. 8.5 Image blur will be caused by any deviation from an unperturbed, low-current trajectory caused by random electron–electron scattering events. A blur profile is constructed from a histogram of the values of Δr , the deviation between Coulomb perturbed and unperturbed electron positions found by mapping the ray-traced electron trajectories to the image plane. Reprinted from [8.22], with permission from Elsevier

graphically in Fig. 8.5, in which two random interactions alter the trajectory of an imaging electron. By projecting the undeviated path of the detected electron back to the specimen plane, the displacement, Δr , gives a measure of the image blur. Figure 8.6 shows a blur profile calculated for conditions similar to those encountered during current DTEM experiments [8.22, 68]: 2×10^4 200-keV electrons with a peak current of 10^6 electrons in 1 ns and propagated through one stage of magnification ($\approx 6.2 \times$) with an objective lens focal length of 2.5 mm, assuming a crossover at the specimen of $1 \mu\text{m}$ diameter and a divergence half angle of 10 mrad. The full-width at half-maximum (FWHM) of the displacement is nearly 19 nm for these conditions. Stochastic blurring will increase with electron density and propagation time of a pulse, and a beam with higher peak current will exhibit increased blur for the same electron optical configuration shown in Fig. 8.6. As well, this blur profile is for a single stage of magnification, and blurring effects will occur at all stages and be especially severe at crossovers, where the electron density and likelihood of random electron–electron interactions is highest. This reveals the significance of stochastic blur on degrading the resolution, and this effect may be the single most important limitation for spatial resolution in DTEM. This resolution limit will depend strongly on beam current and voltage; the number, position, and convergence angle of crossovers; and the positions and degrees of magnification at every image plane. Stochastic blur cannot be completely eliminated, as the electron pulse must have high density at the specimen. For imaging, the back focal plane of the objective lens will have high electron density as the electrons are imaged into disks in reciprocal space [8.22, 68]. This degradation to the resolution limit

may be reduced by changing the lens excitations in the intermediate/projector lens system.

The energy spread of the electrons, ΔE , is expected to be large in the DTEM, because of enhanced Boersch effects at high currents [8.41]. The Boersch effect increases the energy spread of a charged particle beam by coupling the lateral and longitudinal degrees of freedom via statistical electron–electron interactions [8.66–68] and will interact with the objective lens chromatic aberration, C_C , to limit resolution. This process saturates when all degrees of freedom are in thermal equilibrium. Saturation energy depends on accelerating voltages and convergence angles [8.67]. Estimates suggest this energy may saturate in the early part of the column, and that it may be responsible for much of the energy spread measured by *Bostanjoglo et al.* [8.69]. They measured ΔE of 8.7 eV for the prototype DTEM at TU Berlin and used Loeffler’s formalism [8.70] to estimate a value of 7.6 eV for the energy spread due to the Boersch effect.

The spatial resolution achieved in the DTEM is strongly dependent on the signal-to-noise ratio needed to discern a feature at a desired resolution. DTEM is generally signal-limited, so the brightness of the source will have a large impact on the performance of single-pulse electron-imaging instruments. A high-brightness electron source is required to attain high fluence with nearly parallel illumination, as angular spread in the condensed beam tends to wash out the high spatial-frequency information [8.71]. The brightness of the source, B_{source} may be defined as

$$B_{\text{source}} = \frac{Ne}{(\pi r^2)(\pi \alpha^2) \Delta t}, \quad (8.4)$$

where N is the number of electrons in the pulse, e is the electron charge, r is the transverse pulse radius, α

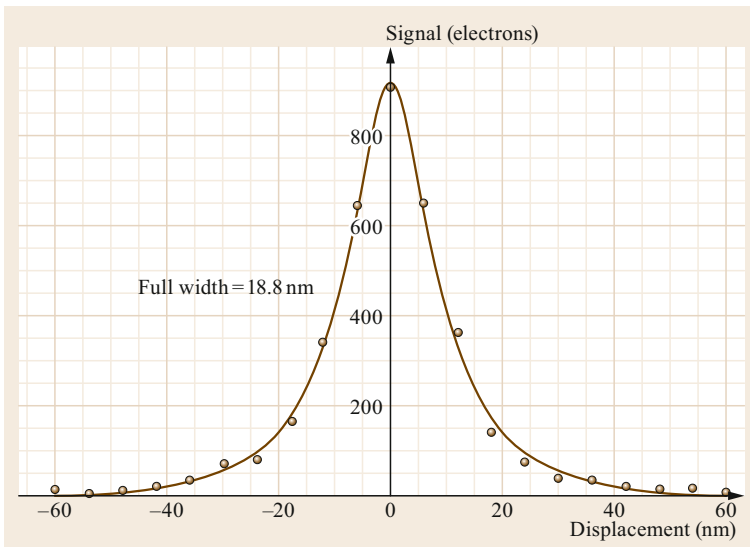


Fig. 8.6 A blur profile for 2×10^4 200-keV electrons with a peak current corresponding to 10^6 electrons in 1 ns, with a $1\text{-}\mu\text{m}$ -diameter crossover at the sample and 10 mrad divergence half-angle, propagated through one magnification stage with an objective focal length of 2.5 mm and $\approx 6.2 \times$ magnification. Reprinted from [8.22], with permission from Elsevier

is the local convergence semiangle, and Δt is the pulse duration [8.25].

For a fixed accelerating voltage, B_{source} is ideally constant as the pulse propagates in the TEM column, though in reality, electron–electron interactions (global space charge) and lens aberrations will degrade the brightness. When considering instrument performance, it is convenient to introduce the coherent fluence, N_C , as a figure of merit. The coherent fluence is the number of electrons per transverse coherence area per pulse, combining the number of electrons in a pulse ($B_{\text{source}}\Delta t$) with the variation of the brightness with accelerating voltage

$$N_C = \frac{N\lambda^2}{r^2\alpha^2} = \frac{\pi^2 B_{\text{source}}\Delta t}{e} \quad (8.5)$$

where λ is the electron wavelength. N_C is a convenient figure of merit because of its relationship to the lateral coherence, $r_C = \lambda/\alpha$, and because it is nearly conserved during propagation of the pulse in the column. N_C is conserved with respect to focusing, apertures, acceleration, and space-charge effects, though aberrations and incoherent scattering can degrade it. Calculations of instrument performance [8.25] relative to N_C are shown in Fig. 8.7, using 10-ns and 1- μs pulse lengths and a standard transfer function for phase and amplitude contrast in a partially coherent conventional TEM (see [52] for details). The simulation includes curves for phase and amplitude contrast as well as incoherent imaging modes (such as HAADF and mass-thickness), for which α is held to a large constant value. On the basis of the simulation, incoherent imaging with a 10-nm pulse should achieve resolution of a few nanometers in a sample with 100% contrast, which is of the correct order of magnitude for the highest demonstrated resolution in the DTEM at LLNL. Using a 15-ns electron pulse, a spatial resolution better than 20 nm was achieved using a calibration specimen of Au-C layers [8.24], which exhibited exemplary mass-thickness contrast, as shown in Fig. 8.8. As in conventional TEM, the attainable spatial resolution is specimen-dependent, and the resolution during processes of interest in many materials will be considerably lower than the maximum achievable resolution. Nonetheless, image resolutions on the order of a few tens of nanometers have been routinely achieved for a variety of liquid-to-solid [8.35, 38, 72, 73] and amorphous-to-crystalline [8.33, 37, 74] phase transitions, and the high current and spatial coherence of the pulsed electron beam are more than sufficient for dynamical contrast imaging of microstructural features such as stacking faults and dislocations (Fig. 8.8). The simulations suggest that resolution as

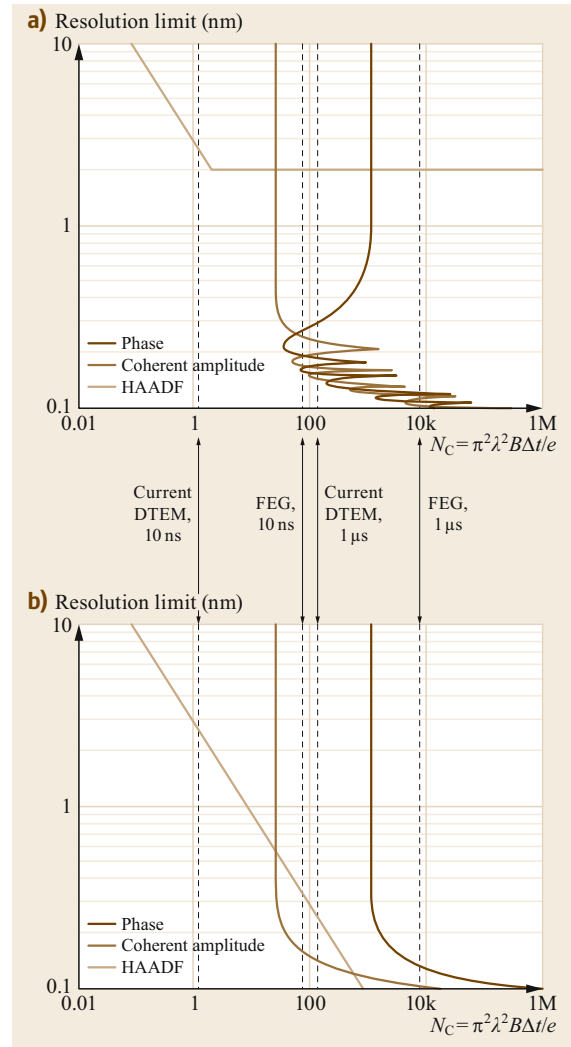


Fig. 8.7a,b C_s -limited (a) and C_s -corrected (b) DTEM resolution limits as a function of the scaled product of brightness and pulse duration. Parameters are 200-keV electrons, $C_s = 2$ mm (a), $5 \mu\text{m}$ (b), $C_C = 2$ mm, $\Delta E = 3$ eV, DTEM brightness $3 \times 10^7 \text{ A cm}^{-2} \text{ sr}^{-1}$, FEG brightness $2 \times 10^9 \text{ A cm}^{-2} \text{ sr}^{-1}$. For ideal samples with 100% contrast; curves for real samples will be shifted to the right. Vertical dashed lines are N_C values for four scenarios, as indicated between the plots. From [8.25], reproduced with permission

high as 0.3 nm can be attained with C_s -limited coherent imaging modes by lengthening the electron pulse to 1 μs , and C_s correction may improve this further. However, the simulations do not include global space-charge effects and stochastic blurring, which will limit the resolution in practice.

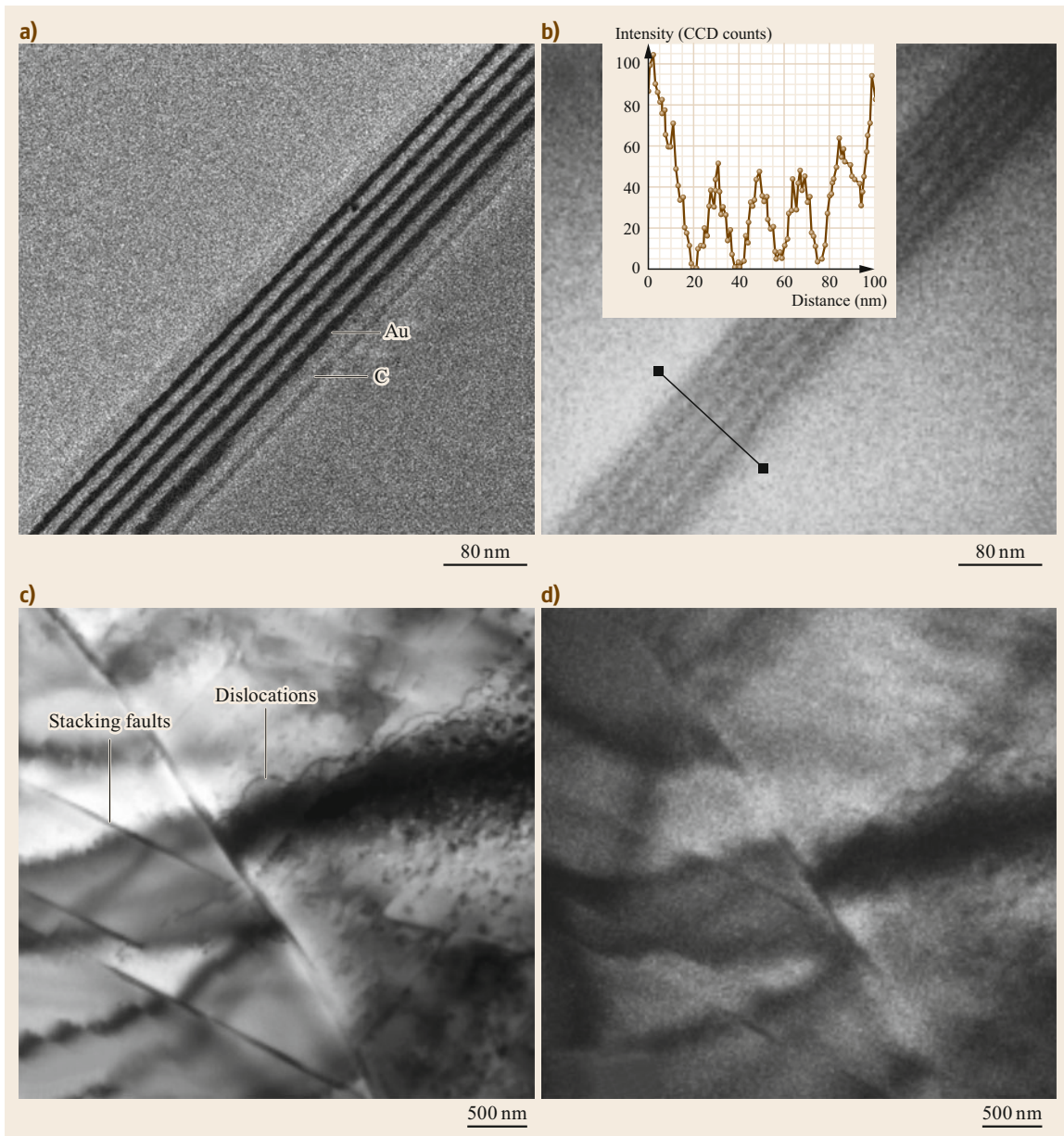


Fig. 8.8 (a) Conventional continuous wave (CW) bright-field TEM image of an Au-C multilayer foil with individual layer thicknesses of ≈ 10 nm, for comparison with (b) a 15-ns pulsed DTEM image of the same multilayer foil. The layers are clearly resolved in the pulsed image. The *inset line profile* in (b) shows the pixel intensity across the multilayer, with the intensity from the layers visible above the background, indicating that the resolution is ≈ 10 nm. (c) CW bright-field TEM image of a stainless steel microstructure, including dislocations and stacking faults, for comparison with (d) a 15-ns pulsed image of the stainless steel microstructure. Despite the difference in exposure times of nearly eight orders of magnitude, most of the microstructural features in the CW image are visible in the pulsed image. These images were not processed apart from standard dark count and flat-field corrections. (a,b) reprinted from [8.24], with permission from Elsevier. (c,d) reprinted from [8.27], with the permission of AIP Publishing

The fluence at the sample can, in principle, be improved by increasing magnification and reducing the area of illumination, but the time-dependent radiation sensitivity of a specimen may limit the usable current density, such that the practical resolution limit has a dependence on the sensitivity of the specimen to electron beam damage. In conventional TEM, 1 μA of current at the specimen is extremely high, corresponding to roughly 1 electron per 160 fs with an axial spacing of $\approx 33 \mu\text{m}$ at 200 keV. Plasmon lifetimes are in the fs range, while TEM samples are typically less than 200 nm thick, so the sample has sufficient time to relax between electron transits (apart from heating and radiation damage). The theory of electron–specimen interactions in conventional TEM uses the assumption of one electron in the specimen at a time. Since instantaneous currents in the DTEM are orders of magnitude higher than in a conventional TEM, many more than one electron may be in the sample at a given time. At high current density, each electron may encounter previously excited plasmons as it transits the specimen. In addition to degrading the spatial resolution, the high DTEM current density may cause new damage mechanisms, which will be considered in Sect. 8.2.1 *Damage in the DTEM*.

Finally, image resolution may be impacted by pro-saic issues. Whereas low-frequency vibrations and high-voltage instabilities can affect conventional TEM resolution, they are not a significant concern during the nanosecond DTEM pulsed imaging due to the short exposure times. However, the triggering of a phase transformation (or the transformation itself) may cause the specimen to move rapidly during an exposure or between image frames. For laser-induced experiments, the sample may distort due to local heating, and for both laser- and mechanical-triggered processes, the specimen may move vertically and thus out of focus. These effects may be mitigated by appropriate design of the specimen geometry and the experimental setup.

Damage in the DTEM

Because of the inelastic scattering of electrons in TEM, a large amount of energy (typically tens of eV per primary electron) may be deposited in the sample. For continuous electron exposure used in standard TEM, damage is linearly related to the total radiation dose [8.75, 76], but the extremely high dose rate during a DTEM pulse raises the possibility of new radiation damage mechanisms and the time dependence of radiation damage must be considered.

Since the timescale of the electron pulse can be comparable to the thermal diffusion time, specimen heating may be a more significant issue for DTEM than for conventional TEM. The deposited energy

density can be very large. As an example, for water irradiated with $\approx 200\text{-keV}$ electrons at a density of 10 electrons/ \AA^2 (a typical density for cryoEM) in a single pulse, an estimate of the inelastic cross-section [8.75] results in a deposited energy density of about 300 eV/ nm^3 , about 10 eV per water molecule. For a Gaussian beam with 1/e radius of 100 nm and 1/e half-width of 1 ns in water, assuming only standard thermal diffusion using room temperature constants, the deposited energy density will reach 90% of the value it would have with no diffusion. For materials with lower heat capacity and larger thermal conductivity, as found in metals, the effect will be much reduced. With the same beam properties, the energy density in an aluminum sample will reach only 5% of the zero diffusion energy density. These results depend strongly on the pulse duration—at a sufficiently short pulse duration with high electron density, sample heating may result in melting, vaporization, or other unintended effects.

In practice, it has been observed that a single condensed DTEM pulse can cause crystallization of amorphous semiconductors and chalcogenide-based phase change alloys, and repeated pulses can melt these materials. During the setup of DTEM experiments, it is often practical to align the microscope first in thermionic mode followed by an alignment in pulsed mode with the unshuttered cathode laser generating electron pulses at the laser repetition rate ($\approx 10\text{ Hz}$). The extreme condition of either a condensed pulse or multiple pulses on the region of interest can be avoided by setting up the experiment on a sacrificial area of the specimen, then moving to a nearby unexposed region of the specimen with the pulsed beam shuttered just prior to data collection. Thus, the only exposure of the specimen in the region of interest is the single electron pulse train used to probe the region after the process has been initiated. Although the instantaneous current density during a DTEM pulse will be several orders of magnitude higher than in conventional TEM, it is only sustained over nanoseconds. By only exposing a specimen to a single DTEM pulse (or pulse train), the total electron dose to the specimen can be lower than in conventional TEM.

Although a wide variety of inorganic and metallic samples can be readily imaged with very high resolution in conventional TEM, for some materials (notably polymers and biomaterials), electron beam damage is the most significant limiting factor in obtaining high-resolution images. One strategy for reducing radiation damage is to lower the total dose [8.77]. As it is possible to expose the specimen with a single electron pulse with a great deal of control, the use of DTEM has been suggested for imaging beam-sensitive samples, such as

fully hydrated biological materials in an aqueous environment, since the total dose from a single DTEM pulse may be less than the dose during conventional TEM, but also because the pulsed imaging would mitigate blurring from Brownian motion or other motion in an aqueous sample.

The high sensitivity of protein crystals to radiation damage is a barrier to high-resolution protein structural characterization [8.78]. In addition to the Brownian motion that may affect conventional TEM imaging, other issues may affect TEM imaging of biological specimens in aqueous environments, including reactive species created in irradiated water, low contrast, intrinsic radiolytic susceptibility, and weakly bound tertiary and quaternary structures of proteins. The use of a short, intense probe pulse to characterize radiation-sensitive specimens before significant damage has occurred has been demonstrated for structural characterization of hydrated proteins with subpicosecond x-ray pulses [8.79]. Although the x-ray pulse ultimately destroys the sample, useful structural data is collected before damage has significantly altered the structure. This diffract-and-destroy [8.80] technique may also be used for photoexcited states (again with many molecules probed), enabling structural characterization of nanoscale biostructural dynamics [8.81]. For this type of structural characterization, a stream of protein crystals must be used to collect the millions of diffraction patterns needed, thus it is analogous to stroboscopic UTEM when considering high-speed electron microscopy techniques.

A diffract-and-destroy type of technique using electron pulses presents its own advantages and challenges (for a comparison of electron and x-ray pulses for this purpose, see [8.82]). Electrons deposit much less energy per inelastic scattering event than x-rays: less than 50 eV per event for electrons [8.75] versus approximately 10 keV for x-rays, and the ratio of inelastic to elastic scattering events is roughly a factor of three smaller for electrons [8.11]. This results in ≈ 1000 times less energy deposited in the sample per unit signal for electrons compared to x-rays. Electrons scatter with 10^4 greater probability than x-rays, which allows imaging with a much lower electron density. However, the electron fluence at the sample is limited because of the degradation of spatial and temporal resolution that occurs at high current densities. The challenge with electron microscopy will be to obtain a pulse of sufficient quality and electron density to obtain a high-resolution image, which is also short enough to avoid damage to the sample during the pulse. This pushes further than the structural x-ray technique, because it demands all the signal come from a single pulse rather than from many pulses (which

would be strictly analogous, but not useful for imaging). Assuming radiation damage can be outrun with electron pulses ≤ 100 fs in duration, a hollow-cone illumination technique has been proposed [8.83] for fast TEM that allows a larger photocathode area (corresponding to an increase in the number of electrons per pulse) but, by reciprocity with scanning transmission electron microscopy (STEM), can provide near-atomic resolution.

Hydrodynamic modeling of single particle diffractive imaging with electrons [8.84] indicates that 4 Å resolution is possible for a molecule of 10 nm radius with 100 keV electrons at a density of 10^7 electrons/(100 nm)², with a pulse width of 2 ps. These single particle models only consider *naked* molecules where the damage mechanism is Coulomb explosion. Although a 2-ps electron pulse width is probably beyond the capability of DTEM using standard electron guns, sub-100 ps pulse widths are not inconceivable at the required electron density. Attaining the necessary spatial and temporal coherence in an ultrashort, high-brightness pulse will probably be very difficult but perhaps within the reach of foreseeable improvements in electron gun technology. Furthermore, the RF (radio frequency) accelerator community is aware of the potential for ultrashort, high-brightness electron guns in electron microscopy [8.85].

Finally, a small amount of experimental evidence exists suggesting that, in some cases, damage may be reduced by the use of pulsed electron exposure even when the total dose of the pulsed exposure is greater than under continuous exposure. *Fryer* [8.86] imaged monolayer films of aromatic hydrocarbons and observed damage thresholds of 90–100 $e/\text{Å}^2$ when using 10- to 100-ms electron pulses, while the damage threshold was 3–4 $e/\text{Å}^2$ when imaged under continuous exposure. This observation suggests that, at least for some materials, pulsed electron imaging may be a means to mitigate beam damage.

8.2.2 UTEM Limitations

UTEM Temporal Resolution

The timescales of the processes that may be probed with UTEM are orders of magnitude shorter than with DTEM. As mentioned previously, the synchronization of the pump and probe lasers are achieved with an optical delay line between a split beam from a single laser, and thus the timing can be accurate to within ≈ 100 fs [8.11].

UTEM Spatial Resolution

Since UTEM operates in a regime where there is ≈ 1 electron per pulse, the spatial resolution does not suffer

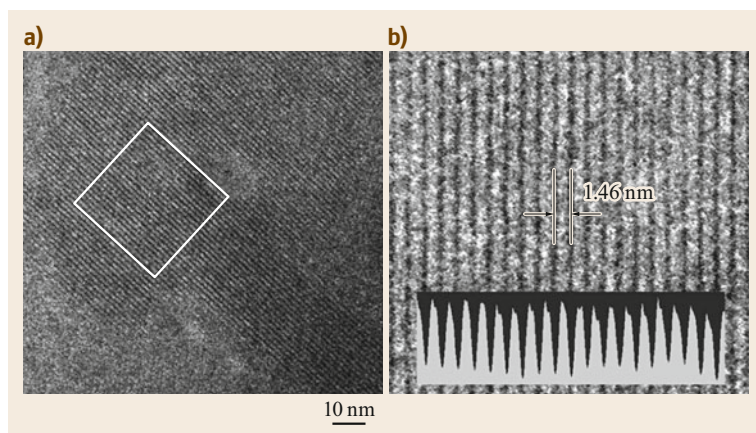


Fig. 8.9 (a) High-resolution phase-contrast UTEM image of an organometallic crystal of chlorinated copper phthalocyanine. (b) A magnified view of the *outlined area* in (a), showing a spatial resolution of 1.46 nm. Reprinted (adapted) with permission from [8.45]. Copyright 2007 American Chemical Society

from degradation due to space charge effects. Spatial resolutions of 1.46 nm in an organometallic crystal (chlorinated copper phthalocyanine) [8.45], shown in Fig. 8.9, and 0.34 nm in images of the planes of graphitic carbon [8.18, 19] have been demonstrated with UTEM, without laser excitation of the specimen. This is comparable to the resolution achieved with conventional high-resolution TEM. Since UTEM images are built up from millions of single-electron pulses, several seconds are required for image acquisition, and specimen drift and high-voltage stability may limit spatial resolution. The loss of resolution during a time-resolved experiment with specimen excitation may come from imperfect reversibility of the process being studied or by movement or damage to the specimen caused by the laser excitation over the millions of pulses required to collect the image [8.87].

UTEM Other Limits

The energy distribution of the electrons in UTEM is limited by the extent to which the incident photon energy exceeds the cathode work function. This may be controlled to better than 0.1 eV [8.45]. This enables electron spectroscopy and also the femtosecond temporal resolution of the technique [8.88].

Since each image in UTEM is formed by integrating millions of electron probes of the pumped specimen, the processes must be repeatable and the specimen must relax to the identical state between shots [8.22]. Thus, UTEM is ideally suited for reversible processes that reset rapidly, such as excitations of plasmon-polariton fields [8.89], but it is not suited for irreversible processes.

8.3 Applications of High-Speed Electron Microscopy

Before discussing recent applications of both DTEM and UTEM, a brief historical review of high-speed electron imaging is provided, limited to time resolutions of microseconds or less. In the mid-1970s, *Bostanjoglo* et al. [8.43, 86] developed a technique to produce stroboscopic images in TEM using beam blanking. In these pump-probe studies, ultrasonics were used to pump samples and study stroboscopically the fast transitions in the materials [8.47, 90–97].

Stroboscopic diffraction studies were carried out in the early 1980s [8.98–100]. Real-time gas-diffraction experiments were reported in 1984 [8.101]. The first picosecond time-resolved structural studies in the solid state occurred in the early 1980s with a streak camera used as the basis of a diffraction instrument [8.4, 5]. This led to the first picosecond time-resolution observation of a phase transition in Al [8.6]. In the late

1980s, pulsed photocathode [8.102], multiframe movies [8.103], and dynamic imaging were demonstrated at TU Berlin [8.104]. In the 1990s there was work in gas-phase energy transfer [8.105], superheating of lead, and structural dynamics [8.106]. The techniques were applied to complex transient phenomena including the dynamics of cyclohexadiene [8.8], photodissociation [8.107], direct observation of ultrafast thermal lattice expansion (Ag) on picosecond timescales [8.108], melting of amorphous Si [8.9], phase explosion in metal films [8.109], and melting of Al [8.110].

TEM with high time resolution began at TU Berlin in the 1970s with stroboscopic imaging of periodic processes using a periodically deflected electron beam [8.43]. In this configuration, time resolutions of 200 ps were achieved for periodic processes up to 100 MHz [8.111]. This technique was applied to ultra-

sonically driven disruption of crystals and magnetoelastic effects [8.112, 113] and magnetic field-induced oscillations of the domain magnetization, of domain walls, and of their substructures [8.91, 111, 114]. After 1980, the instrument was modified to study nonperiodic processes. That instrument operated in three modes:

1. Selected-area image-intensity streaking provided time resolution of 3 ns and selected areas ≥ 500 nm [8.94]. This was applied to studies of electron- [8.92, 94, 95] and laser-induced [8.115, 116] crystallization of metals and semiconductors, thermocapillary oscillations [8.117, 118], and solidification of laser-induced melts [8.109, 117, 118].
2. Streaked imaging was used to study solidification [8.117], flow [8.117, 119, 120], and evaporation [8.119, 120] of laser-pulsed samples.
3. High-speed imaging and three-frame movies with temporal/spatial resolutions of 10 ns/200 nm, interpulse spacing > 20 ns [8.41], and diffraction with time resolution of 10 ns were demonstrated [8.41].

Several techniques were employed to achieve the high time resolution, including gating the electron detector [8.104, 119, 121], rapid beam blanking [8.122], laser-induced thermal emission [8.69, 123–126], and finally laser-induced photoemission [8.41, 127]. Nanosecond time resolution studies using the photoemission source were carried out on hydrodynamic instabilities caused by chemocapillary, thermocapillary [8.128], and mechanical stresses [8.129]. Phase explosion and plasma formation of highly superheated metals were studied at the same time resolution [8.109, 130].

Since the early to mid-2000s, *Zewail* and researchers at Caltech have pushed the temporal resolution of the stroboscopic approach with UTEM to the subpicosecond regime with femtosecond lasers [8.17–19], while researchers at LLNL have advanced the single-shot approach with DTEM using single electron pulses in the nanosecond regime [8.21–25, 28]. Applications of these two complementary techniques, each optimized for a particular, broad class of experiments, will be discussed separately in Sects. 8.3.1 and 8.3.2.

8.3.1 DTEM Applications

As has been discussed, DTEM is optimized to study irreversible processes with nanometer and nanosecond spatial and temporal resolutions. Much of the DTEM work has focused on transient states of strongly driven or highly nonequilibrium phase transformations and measurements of the kinetics of these rapidly evolving processes.

Phase transitions in nanocrystalline Ti [8.31, 131], transient structures and morphologies of moving reaction fronts in Ni/Al reactive multilayer foils (RMLFs) [8.32, 132], studies combining nanocalorimetry with DTEM [8.62], crystallization processes in Ni-Ti metallic glass [8.133], GeTe [8.134, 135] and Ge₂Sb₂Te₅ [8.136] phase-change materials, and amorphous Ge thin films [8.137, 138], rapid solidification in pure Al [8.72] and Al-based [8.35] alloys, in situ heating of Al nanoparticle aggregates [8.139], and pulsed-laser-induced dewetting of Ni [8.140] and Co-Cu [8.34] thin films are examples of studies using single-shot DTEM prior to the implementation of the multiframe-acquisition movie-mode capability. An example of a single-shot time-resolved image series is provided in Fig. 8.10, showing results obtained during crystallization of an amorphous Ge thin film. Single-shot DTEM studies require many experiments to be performed at different time delays on fresh, unirradiated regions of a specimen to quantify the overall statistics of kinetics and evolution of the process of interest. There is inherent variability associated with the single-shot approach to irreversible processes, as there may be small differences in the evolution of the process from experiment to experiment, as well as variation in parameters such as the laser energy used to drive the process.

Movie-mode DTEM was developed to alleviate these issues, providing a multiframe acquisition mode from a single drive-laser event. Examples of movie-mode DTEM experiments are provided in Figs. 8.11 and 8.12 to illustrate the types of data that can be obtained. Figure 8.11 shows crystallization in an amorphous GeTe film, where growth was captured following a single nucleation event. Figure 8.12 shows the rapid solidification of an Al-4 at.% Cu alloy [8.38], with the associated measurements of the kinetics of the transformation. Other applications of movie-mode DTEM include disorder–order transitions in 2D copper-intercalated MoO₃ [8.36], nanoscale condensed-phase reactions with Al and CuO nanoparticles [8.142], propagating fronts in reacting Ti-B nanolaminate films [8.30], crystallization kinetics of amorphous Ge [8.37, 143] and GeSb₆Te phase-change materials [8.74], dewetting of nanoscale Ni thin films on SrTiO₃ substrates [8.56], and rapid solidification of pure Al thin films [8.73].

8.3.2 UTEM Applications

UTEM is optimized to study reversible, highly repeatable processes, reaching atomic-scale spatial resolution with femtosecond temporal resolution, that are induced by optical excitation, including electronic and plas-

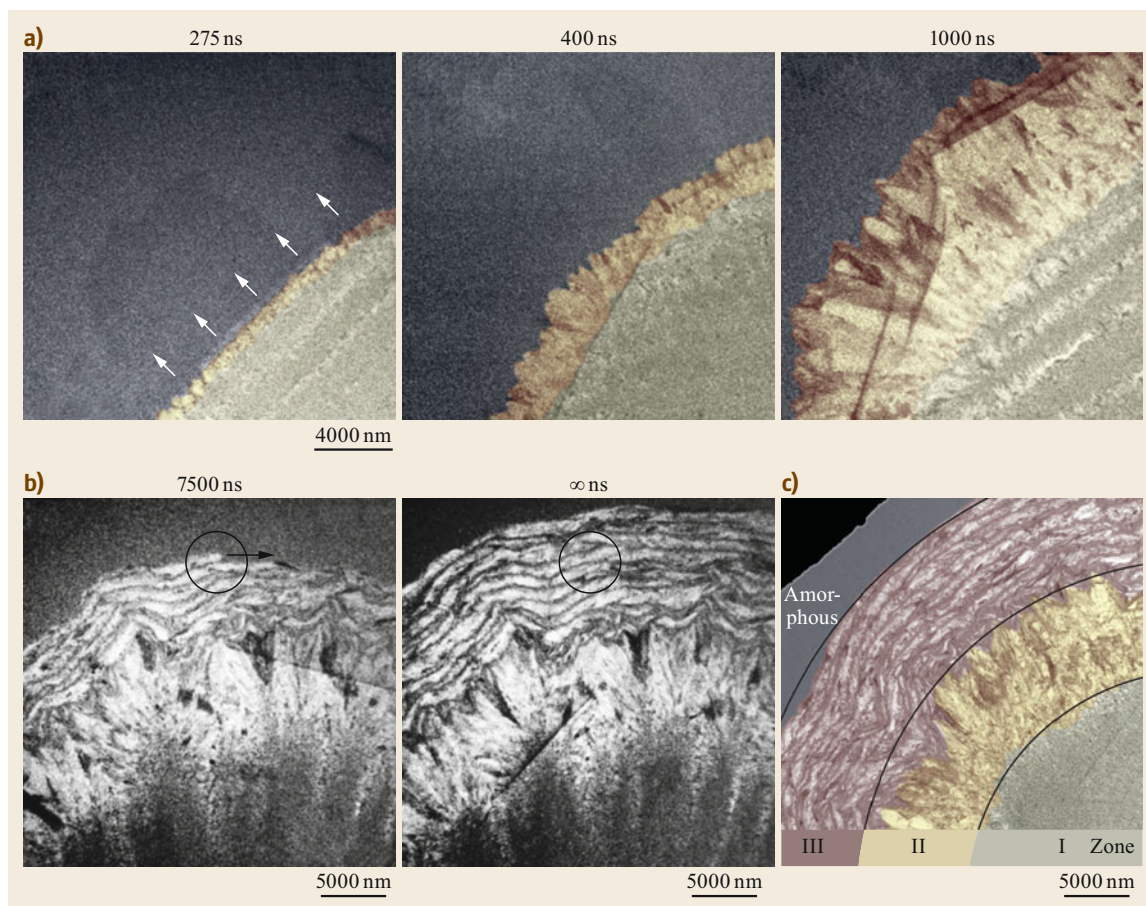


Fig. 8.10a–c Single-shot DTEM image series of the time-evolving microstructure during laser-induced crystallization of amorphous Ge. **(a)** Large, radially elongated crystals grow outwards with a radial velocity of ≈ 8 m/s. **(b)** A banded microstructure composed of layers of elongated crystals that grow azimuthally along the crystallization front. **(c)** A post-mortem image showing the crystalline microstructure, with three zones of growth shown. Zone I is a region of nucleation and growth of nanocrystalline grains. Zone II is comprised of the large, elongated crystals that grow radially outward. The crystallization front is initially flat, then develops microscopically smooth protrusions that show an increasingly faceted appearance at the boundary where growth transitions to Zone III, which is comprised of layers of elongated crystals separated by layers of nanocrystalline grains. Adapted with permission from [8.138]. Copyrighted 2013 by the American Physical Society

monic excitations [8.141] as well as repeatable nanomechanical excitations [8.145–149]. The high temporal resolution of UTEM demands precise (picosecond to femtosecond) synchronization between the specimen pump laser and probing electron pulses. The main focus of UTEM research has been nonequilibrium structural phase transitions, nanoscale phenomena, and biological imaging, with recent additions of electron energy-loss spectroscopy (EELS), energy-filtered UTEM imaging, and scanning transmission UTEM.

Examples of applications of UTEM imaging and diffraction include structural phase transitions in VO_2 [8.150, 151], the dynamics of structural and mor-

phological changes in Au and graphite thin films induced by ultrafast laser heating [8.18], complex nanoscale mechanical phenomena in copper-7,7,8,8-tetracyanoquinodimethane [Cu(TCNQ)] single crystals [8.49, 145], single-crystalline graphite [8.48], Ni-Ti nanostructures [8.152, 153], and nanoscale Si cantilevers [8.149], the heating and cooling dynamics of carbon nanotubes [8.154], photon-induced near-field imaging of carbon nanotubes [8.141], Ag nanowires [8.141], biomimetic protein vesicles [8.155], unstained, unfixed *E. coli* cells [8.155], Ag nanoparticles [8.156], optomechanical phenomena of amorphous silicon nitride at the interface with carbon na-

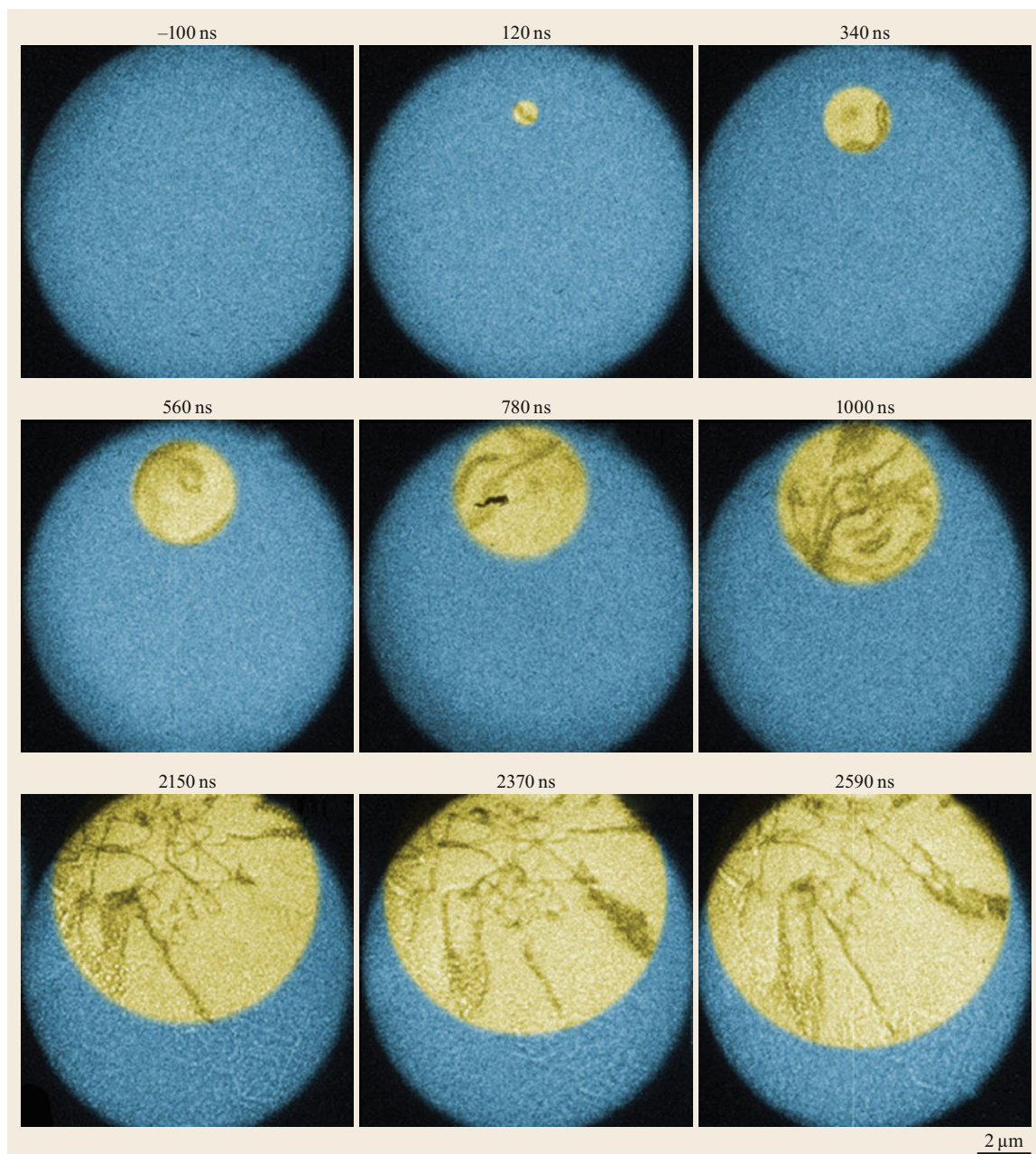


Fig. 8.11 Movie-mode DTEM showing growth of crystalline regions (*false-colored yellow*) into amorphous GeTe (*false-colored blue*) in a nine-image series of 17.5-ns electron pulses after 4.7- μ J laser shots. The time signature in each frame is relative to the time of the peak specimen laser intensity with an uncertainty of ± 3 ns. Adapted from [8.33], with the permission of AIP Publishing

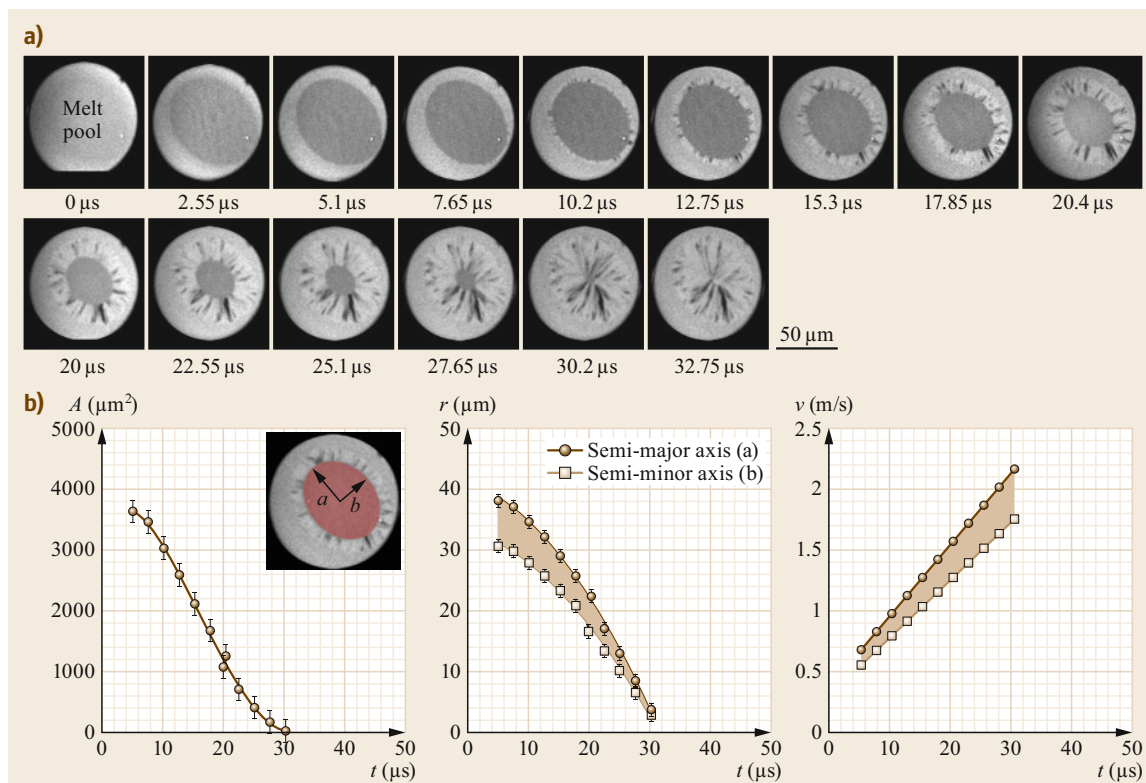


Fig. 8.12 (a) Dynamic time-delay sequence of images recorded during rapid solidification in an Al-4at.%Cu thin-film alloy. The indicated times *below each image* are the delays (in μs) between the peak of the Gaussian laser pulse used to melt the film and the 50-ns electron pulse used to form the image. (b) Time evolution of the (*left*) melt pool area, (*middle*) semi-major and semi-minor axes of the elliptical melt pool, and (*right*) solidification front velocity. The *brown areas* bounded by the semi-major and semi-minor axes represent the ranges of (*middle*) axis length and (*right*) velocity along the solid–liquid interface. Adapted from [8.38]

notubes [8.157], structural dynamics in macromolecular poly(ethylene) oxide (PEO) [8.146], biomechanics of DNA structures [8.158] and amyloid [8.147, 148], transient structures in GeTe phase-change materials [8.159], and the photocatalytic active sites in titanosilicate, $\text{Na}_4\text{Ti}_2\text{Si}_8\text{O}_{22} \cdot 4\text{H}_2\text{O}$ [8.160], imaging of defect-modulated phonon dynamics in WSe_2 and Ge [8.161], and the acousto-plasmonic vibrational dynamics in Au nanorods [8.162]. Examples of UTEM experiments are provided in Figs. 8.13 and 8.14, showing, respectively, photon-induced near-field electron microscopy (PINEM) from a carbon nanotube [8.141] and single-nanoparticle morphology dynamics on spin crossover in a metal-organic framework $\text{Fe}(\text{pyrazine})\text{Pt}(\text{CN})_4$ [8.144].

UTEM has also been used to study irreversible phase transformations, such as amorphous to crystalline transitions in Si [8.163] and martensitic phase-transformation dynamics in Fe [8.164]. In these cases, nanosecond laser pulses were used to achieve adequate

signal for a single image or diffraction pattern acquired from a specific state of the specimen, and the temporal resolution is similar to that of single-shot DTEM. Thus, UTEM can be operated in two modes, a high-temporal-resolution (picosecond to femtosecond) stroboscopic mode for highly reversible processes that can be induced with precisely coordinated pump excitations and a single-shot mode for irreversible processes that can be induced with pulsed-laser heating.

In addition to imaging and diffraction applications, numerous techniques for UTEM have been explored and developed, including ultrafast EELS [8.50, 165, 166], PINEM [8.89, 141, 155, 156, 166–168], ultrafast convergent-beam diffraction [8.169] and Kikuchi nanodiffraction [8.170], ultrafast electron tomography [8.171], ultrafast scanning electron microscopy (SEM) [8.172–174], ultrafast Lorentz electron microscopy [8.175], ultrafast STEM [8.176], ultrafast spectrum imaging [8.177], and ultrafast cryo-electron microscopy [8.178].

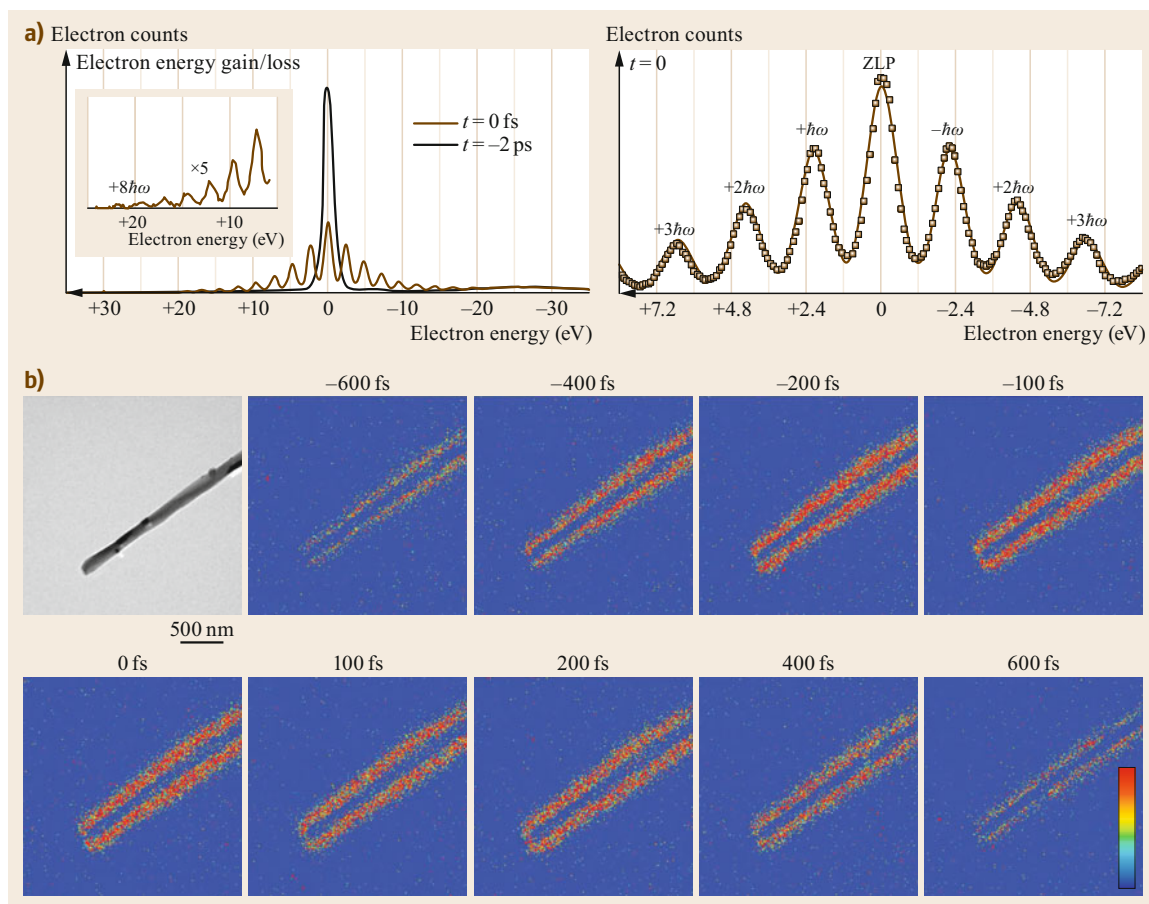


Fig. 8.13 (a) Electron energy spectra of carbon nanotubes irradiated with an intense fs laser pulse at two time delays. (Left) Zero-loss peak (ZLP) of the 200-keV electrons (black curve) acquired when the electron packet arrived prior to the femtosecond laser pulse, with only the plasmon peaks present in the spectrum. The energy spectrum when the laser and electron pulses are coincident ($t = 0$ fs; brown curve) displays the multiple quanta of photon absorption/emission. The inset shows the positive energy-gain region multiplied by 5 for the $t = 0$ spectrum, indicating that absorption of at least eight quanta of photon energy were observed at maximum spatiotemporal overlap. (Right) Magnified view of the $t = 0$ energy spectrum. The energy is given in reference to the loss/gain of photon quanta by the electrons with respect to zero-loss energy. (b) Photon-induced near-field electron microscopy of an individual carbon nanotube. A bright-field TEM image of the nanotube is provided for reference (average diameter across the tube is 147 ± 20 nm). The nine energy-filtered UTEM images were acquired using only electrons that have gained energy (up to $n = 4$) relative to the ZLP. The time of arrival of the electron packet relative to the laser pulse is indicated in the upper left of each image. Images are provided in false color for clarity, with blue indicating regions of the CCD where no counts were recorded (only the $+n\hbar\omega$ region of the spectrum was selected) and red representing the evanescent fields created by the femtosecond pulse around the surface of the nanotube and their decay with time. Adapted from [8.141]

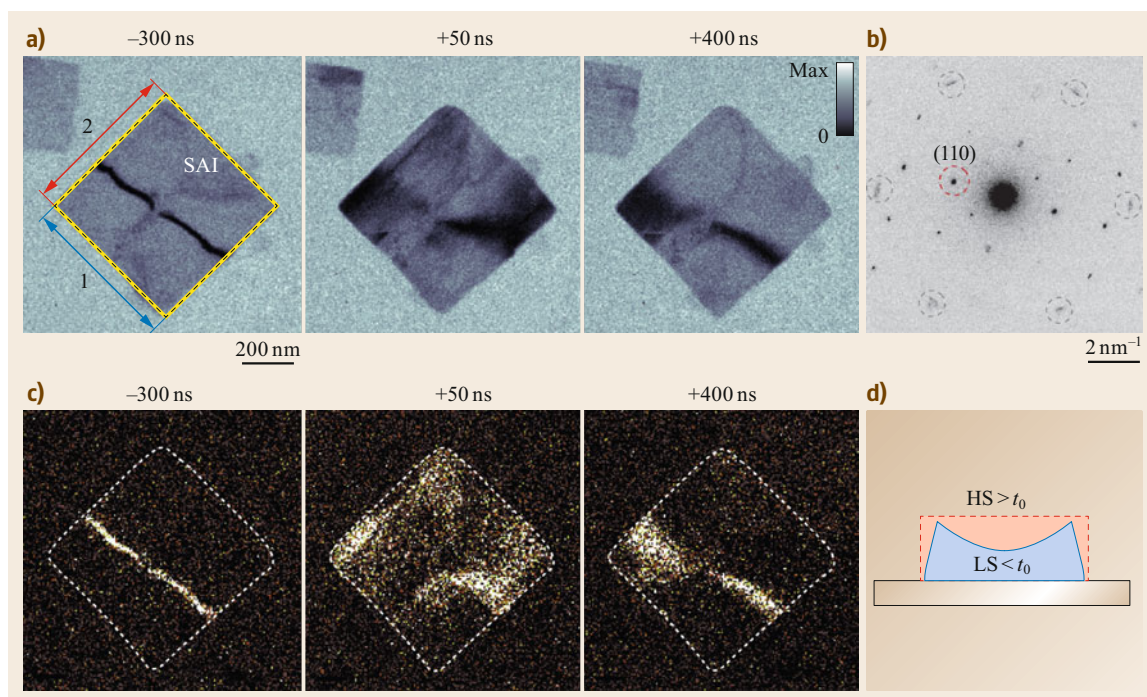


Fig. 8.14a–d Single-nanoparticle morphology dynamics on spin crossover in a metal-organic framework $\text{Fe}(\text{pyrazine})\text{Pt}(\text{CN})_4$. **(a)** Bright-field recorded at three time delays (indicated in *lower right* of images). The *red* and *blue* lines (labeled 1 and 2) refer to the particle directions used to quantify dimensional changes with time, while the *yellow box* (labeled SAI) was used to quantify contrast dynamics (see [8.139] for further details and plots). **(b)** Single-nanoparticle diffraction pattern. **(c)** Corresponding dark-field images at the three time delays. The (110) diffraction peak (*red*) was selected to construct the dark-field images in **(c)** and visualize the contrast dynamics. Diffraction peaks *circled in gray* belong to the supporting graphite substrate. **(d)** Schematic of the morphology dynamics on spin crossover. LS and HS refer to, respectively, diamagnetic low-spin and paramagnetic high-spin states. Prior to laser excitation (before $t = 0$), the nanoparticle shape is buckled/strained, and after $t = 0$ the structure expands and relaxes. Adapted from [8.144]

8.4 Outlook

The evolution of high-speed electron microscopy over the last decade has taken the field to the point of allowing direct visualization of dynamic processes in materials as they unfold on timescales from femtoseconds to microseconds, with spatial resolutions from the atomic scale to tens of nanometers. While this is a significant achievement, there is much room for improvement.

UTEM achieves subpicosecond temporal resolution by accumulating millions or more electron pulses from reversible process cycles, but as this temporal resolution is relaxed the number of pulses required for an image decreases, eventually reaching the single-shot regime of DTEM with its current limits of ≈ 10 -ns temporal and 10-nm spatial resolutions for irreversible processes [8.30]. Future radio frequency (RF) photoinjectors with MeV electron beam energies may allow for

single-shot imaging with picosecond temporal resolution and ≈ 10 -nm spatial resolution, representing an improvement of 3 orders of magnitude compared to current single-shot DTEM temporal resolution [8.54], though their use in single-shot imaging systems may be limited to incoherent contrast mechanisms [8.30]. Eventually, the temporal regimes of all time-resolved techniques may overlap into a continuum, with the method of choice depending on the necessary spatiotemporal resolution for the process of interest.

8.4.1 Improving and Bridging Temporal Resolutions

Pulse Compression for Single-Shot Imaging

To recap, the electron pulse duration at the sample is equal to the single-shot time resolution of the DTEM.

At present, this is essentially equal to the cathode laser-pulse duration and is dictated by the experiment's fluence requirements and the electron gun brightness. However, many methods exist for longitudinally compressing an electron pulse, many of them developed by the accelerator community for high-voltage RF electron guns. These involve passing the pulse through specialized elements such as a microwave cavity operating at a carefully chosen phase [8.179–181], or static magnetic fields in a chicane [8.182–184], α -shaped magnet [8.185], or other pulse-compressing arrangement [8.186]. These devices are routinely used to compress multimegavolt pulses of $\approx 10^{10}$ electrons down to picosecond or shorter durations, with normalized emittance values of $\approx 1 \mu\text{m rad}$ and $\approx 1\%$ energy spreads. The desired DTEM parameter space is very different, of order 200 keV, 10^8 electrons, less than $0.1 \mu\text{m rad}$ emittance, and an energy spread of order one part in 10^5 . Without increasing the effective brightness of the electron source by crowding the electrons into a shorter pulse, there are many measurements (requiring a combination of high fluence, small convergence angle, and high time resolution) that will simply be impossible.

Even then, there will be fundamental limits. Electrons are fermions and can be compressed to a finite density only in six-dimensional phase space [8.66]. Passive transformations to the electron pulse (e. g., acceleration, lens action, and most compression methods) can change only the shape of the phase space envelope and not its density [8.66, 187]. Thus, every compression method that does not actually refrigerate the electron pulse will involve trading off one design parameter against another. Ultracold sources decrease the emittance, increase the transverse coherence length, and increase the brightness [8.188]. To that end, significant effort has been devoted to developing ultracold electron sources [8.188–199], which potentially could provide increased brightness with sufficient coherence for single-shot imaging of microstructural details or even atomic-scale structure [8.30].

Relativistic Beams

High time resolution can also be achieved by increasing the accelerating voltage of the electrons. The application of RF photoinjectors with MeV electron beams offers the advantages of an extremely high brightness, high acceleration gradient ($\approx 100 \text{ MV/m}$, compared to $< 10 \text{ MV/m}$ in a conventional TEM due to arcing in the gun) [8.54], high final beam energy ($\approx 3\text{--}5 \text{ MeV}$), and high beam charge (up to a few nC or 10^{10} electrons per pulse) [8.54]. These sources have enabled the

development of x-ray free-electron lasers [8.200]. The electron beams become relativistic in a few centimeters, quickly reducing the space-charge force repulsion. (Space-charge force is reduced for high-energy beams. Several books derive the space-charge equations for both longitudinal and transverse space charge, showing the force varies as the Lorentz factor γ^{-2} [8.201, 202].)

While these sources have yet to be implemented in electron-based imaging instruments, such as a time-resolved MeV TEM, the last decade has seen significant progress toward using RF photocathode guns for ultrafast electron diffraction [8.15, 203–208]. There are currently ongoing research efforts to develop MeV TEM with picosecond temporal resolution and $\approx 10\text{-nm}$ spatial resolution [8.54, 55, 209, 210]. Prototype instruments have been developed [8.55, 211], and simulations [8.54] have shown that it is possible to generate a 5-MeV electron beam with 1 pC of charge, 3 ps RMS (root mean square) width, $< 10 \text{ nm}$ normalized emittance, and $< 1 \mu\text{m rms}$ spot size at the sample.

Bridging Temporal Resolutions

Temporal resolutions from femtoseconds to nanoseconds are not always required. For many applications, continuous acquisition of multi-kHz frame rates is more than sufficient, representing a gap between high-speed movie-mode DTEM and the millisecond timescales of conventional in situ TEM. While still early in its development, solutions to bridging this temporal gap using a deflector system, as used in movie-mode DTEM, are underway, potentially enabling continuous-acquisition in situ experimentation on microsecond timescales to enhance the data throughput of in situ and analytical (S)TEM [8.30, 212].

8.4.2 Further Directions for High-Speed Electron Microscopy

Future directions of high-speed electron microscopy also include time-resolved imaging of processes under conditions that are used in real-world applications, such as in specific gaseous [8.213, 214] or liquid [8.215] environments or under extreme mechanical loading conditions [8.63, 64], topics that are highly studied using conventional in situ TEM techniques. The ability to acquire images with high temporal resolution under conditions that are used in real-world applications would provide insights to materials processes that currently cannot be obtained, and efforts to characterize the limits of these in situ techniques using DTEM are in the early stages.

8.5 Conclusions

The interest in ultrafast science continues to grow, and high-speed electron microscopy has emerged over the last decade into a well-established field. Ongoing developments in both DTEM and UTEM are moving in situ TEM toward becoming a capability that can provide observations of complex and transient materials phenomena at relevant length and time scales for the processes of interest, spanning orders of magnitude (i. e., pico-, nano-, micro-, meso-) in space and time. As well, observations of these processes are now becoming possible under conditions that are used in real-world applications. Even with the recent rapid development in DTEM and UTEM, significant improvements are possible, including brighter electron sources,

pulse compression, relativistic accelerating voltages, and an eventual intersection of techniques to encompass a temporal domain that bridges the current gaps that exist between UTEM, DTEM, and conventional in situ TEM.

Acknowledgments. This work was performed under the auspices of the U.S. Department of Energy by Lawrence Livermore National Laboratory (LLNL) under Contract No. DE-AC52-07NA27344. Activities and personnel at LLNL were supported by the U.S. Department of Energy, Office of Science, Office of Basic Energy Sciences, Division of Materials Science and Engineering under FWP SCW0974.

References

- 8.1 P.B. Hirsch: Direct observations of dislocations by transmission electron microscopy: Recollections of the period 1946–56, *Proc. Royal Soc. A* **371**, 160 (1980)
- 8.2 P.B. Hirsch: Direct observations of moving dislocations: Reflections on the thirtieth anniversary of the first recorded observations of moving dislocations by transmission electron microscopy, *Mater. Sci. Eng.* **84**, 1 (1986)
- 8.3 P.B. Hirsch, R.W. Horne, M.J. Whelan: Direct observations of the arrangement and motion of dislocations in aluminium, *Philos. Mag.* **1**, 677 (1956)
- 8.4 G. Mourou, S. Williamson: Picosecond electron-diffraction, *Appl. Phys. Lett.* **41**, 44 (1982)
- 8.5 S. Williamson, G. Mourou: Electron-diffraction in the picosecond domain, *Appl. Phys. B* **28**, 249 (1982)
- 8.6 S. Williamson, G. Mourou, J.C.M. Li: Time-resolved laser-induced phase-transformation in aluminum, *Phys. Rev. Lett.* **52**, 2364 (1984)
- 8.7 H.E. Elsayed-Ali, J.W. Herman: Picosecond time-resolved surface-lattice temperature probe, *Appl. Phys. Lett.* **57**, 1508 (1990)
- 8.8 R.C. Dudek, P.M. Weber: Ultrafast diffraction imaging of the electrocyclic ring-opening reaction of 1,3-cyclohexadiene, *J. Phys. Chem. A* **105**, 4167 (2001)
- 8.9 C.Y. Ruan, F. Vigliotti, V.A. Lobastov, S.Y. Chen, A.H. Zewail: Ultrafast electron crystallography: Transient structures of molecules, surfaces, and phase transitions, *Proc. Natl. Acad. Sci. USA* **101**, 1123 (2004)
- 8.10 C.Y. Ruan, V.A. Lobastov, F. Vigliotti, S.Y. Chen, A.H. Zewail: Ultrafast electron crystallography of interfacial water, *Science* **304**, 80 (2004)
- 8.11 B.J. Siwick, J.R. Dwyer, J.E. Jordan, R.J.D. Miller: Femtosecond electron diffraction studies of strongly driven structural phase transitions, *Chem. Phys.* **299**, 285 (2004)
- 8.12 Gatan Inc.: <http://www.gatan.com/products/tem-imaging-spectroscopy> (2017)
- 8.13 P. Emma, R. Akre, J. Arthur, R. Bionta, C. Bostedt, J. Bozek, A. Brachmann, P. Bucksbaum, R. Coffee, F.-J. Decker, Y. Ding, D. Dowell, S. Edstrom, A. Fisher, J. Frisch, S. Gilevich, J. Hastings, G. Hays, P. Hering, Z. Huang, R. Iverson, H. Loos, M. Messerschmidt, A. Miahnahri, S. Moeller, H.-D. Nuhn, G. Pile, D. Ratner, J. Rzepiela, D. Schultz, T. Smith, P. Stefan, H. Tompkins, J. Turner, J. Welch, W. White, J. Wu, G. Yocky, J. Galayda: First lasing of an ångstrom-wavelength free-electron laser, *Nat. Photonics* **4**, 641 (2010)
- 8.14 T. Ishikawa, H. Aoyagi, T. Asaka, Y. Asano, N. Azumi, T. Bizen, H. Ego, K. Fukami, T. Fukui, Y. Furukawa, S. Goto, H. Hanaki, T. Hara, T. Hasegawa, T. Hatsui, A. Higashiya, T. Hirano, N. Hosoda, M. Ishii, T. Inagaki, Y. Inubushi, T. Itoga, Y. Joti, M. Kago, T. Kameshima, H. Kimura, Y. Kirihaara, A. Kiyomichi, T. Kobayashi, C. Kondo, T. Kudo, H. Maesaka, X.M. Maréchal, T. Masuda, S. Matsubara, T. Matsumoto, T. Matsushita, S. Matsui, M. Nagasono, N. Nariyama, H. Ohashi, T. Ohata, T. Ohshima, S. Ono, Y. Otake, C. Saji, T. Sakurai, T. Sato, K. Sawada, T. Seike, K. Shirasawa, T. Sugimoto, S. Suzuki, S. Takahashi, K. Takebe, A. Tokuhisa, H. Tomizawa, K. Tono, S. Wu, M. Yabashi, M. Yamaga, A. Yamashita, K. Yanagida, C. Zhang, T. Shinzaki, H. Kitamura, N. Kumagai: A compact x-ray free-electron laser emitting in the sub-ångstrom region, *Nat. Photonics* **6**, 540 (2010)
- 8.15 S.P. Weathersby, G. Brown, M. Centurion, T.F. Chase, R. Coffee, J. Corbett, J.P. Eichner, J.C. Frisch, A.R. Fry, M. Gühr, N. Hartmann, C. Hast, R. Hettel, R.K. Jobe, E.N. Jongewaard, J.R. Lewandowski, R.K. Li, A.M. Lindenbergh, I. Makasyuk, J.E. May, D. McCormick, M.N. Nguyen, A.H. Reid, X. Shen, K. Sokolowski-Tinten, T. Vecchione, S.L. Vetter, J. Wu, J. Yang, H.A. Dürr, X.J. Wang: Mega-electron-volt ultrafast electron diffraction at SLAC National Accelerator Laboratory, *Rev. Sci. Instrum.* **86**, 073702 (2015)

- 8.16 V.A. Lobastov, R. Srinivasan, A.H. Zewail: Four-dimensional ultrafast electron microscopy, *Proc. Natl. Acad. Sci. USA* **102**, 7069 (2005)
- 8.17 A.H. Zewail: 4D ultrafast electron diffraction, crystallography, and microscopy, *Annu. Rev. Phys. Chem.* **57**, 65 (2006)
- 8.18 B. Barwick, H.S. Park, O.H. Kwon, J.S. Baskin, A.H. Zewail: 4D imaging of transient structures and morphologies in ultrafast electron microscopy, *Science* **322**, 1227 (2008)
- 8.19 A.H. Zewail: Four-dimensional electron microscopy, *Science* **328**, 187 (2010)
- 8.20 A.H. Zewail, J.M. Thomas: *4D Electron Microscopy* (Imperial College Press, London 2010)
- 8.21 T. LaGrange, M.R. Armstrong, K. Boyden, C.G. Brown, G.H. Campbell, J.D. Colvin, W.J. DeHope, A.M. Frank, D.J. Gibson, F.V. Hartemann, J.S. Kim, W.E. King, B.J. Pyke, B.W. Reed, M.D. Shirk, R.M. Shuttlesworth, B.C. Stuart, B.R. Torralva, N.D. Browning: Single-shot dynamic transmission electron microscopy, *Appl. Phys. Lett.* **89**, 044105 (2006)
- 8.22 M.R. Armstrong, K. Boyden, N.D. Browning, G.H. Campbell, J.D. Colvin, W.J. DeHope, A.M. Frank, D.J. Gibson, F. Hartemann, J.S. Kim, W.E. King, T.B. LaGrange, B.J. Pyke, B.W. Reed, R.M. Shuttlesworth, B.C. Stuart, B.R. Torralva: Practical considerations for high spatial and temporal resolution dynamic transmission electron microscopy, *Ultramicroscopy* **107**, 356 (2007)
- 8.23 M.R. Armstrong, B.W. Reed, B.R. Torralva, N.D. Browning: Prospects for electron imaging with ultrafast time resolution, *Appl. Phys. Lett.* **90**, 114101 (2007)
- 8.24 T. LaGrange, G.H. Campbell, B. Reed, M. Taheri, J.B. Pesavento, J.S. Kim, N.D. Browning: Nanosecond time-resolved investigations using the *in situ* of dynamic transmission electron microscope (DTEM), *Ultramicroscopy* **108**, 1441 (2008)
- 8.25 B. Reed, M.R. Armstrong, N.D. Browning, G.H. Campbell, J.E. Evans, T. LaGrange, D.J. Masiel: The evolution of ultrafast electron microscope instrumentation, *Microsc. Microanal.* **15**, 272 (2009)
- 8.26 G.H. Campbell, T. LaGrange, J.S. Kim, B.W. Reed, N.D. Browning: Quantifying transient states in materials with the dynamic transmission electron microscope, *J. Electron Microsc.* **59**, S67 (2010)
- 8.27 B.W. Reed, T. LaGrange, R.M. Shuttlesworth, D.J. Gibson, G.H. Campbell, N.D. Browning: Solving the accelerator-condenser coupling problem in a nanosecond dynamic transmission electron microscope, *Rev. Sci. Instrum.* **81**, 053706 (2010)
- 8.28 T. LaGrange, B.W. Reed, M.K. Santala, J.T. McKeown, A. Kulovits, J.M. Wiezorek, L. Nikolova, F. Rosei, B.J. Siwick, G.H. Campbell: Approaches for ultrafast imaging of transient material processes in the transmission electron microscope, *Micron* **43**, 1108 (2012)
- 8.29 G.H. Campbell, J.T. McKeown, M.K. Santala: Time resolved electron microscopy for *in situ* experiments, *Appl. Phys. Rev.* **1**, 041101 (2014)
- 8.30 T. LaGrange, B.W. Reed, D.J. Masiel: Movie-mode dynamic electron microscopy, *MRS Bulletin* **40**, 22 (2015)
- 8.31 T. LaGrange, G.H. Campbell, J.D. Colvin, B. Reed, W.E. King: Nanosecond time resolved electron diffraction studies of the $\alpha \rightarrow \beta$ transition in pure Ti thin films using the dynamic transmission electron microscope (DTEM), *J. Mater. Sci.* **41**, 4440 (2006)
- 8.32 J.S. Kim, T. LaGrange, B.W. Reed, M.L. Taheri, M.R. Armstrong, W.E. King, N.D. Browning, G.H. Campbell: Imaging of transient structures using nanosecond in situ TEM, *Science* **321**, 1472 (2008)
- 8.33 M.K. Santala, B.W. Reed, S. Raoux, T. Topuria, T. LaGrange, G.H. Campbell: Irreversible reactions studied with nanosecond TEM movies: Laser crystallization of phase change materials, *Appl. Phys. Lett.* **102**, 174105 (2013)
- 8.34 J.T. McKeown, Y. Wu, J.D. Fowlkes, P.D. Rack, G.H. Campbell: Simultaneous in-situ synthesis and characterization of Co@Cu core-shell nanoparticle arrays, *Adv. Mater.* **27**, 1060 (2014)
- 8.35 J.T. McKeown, A. Kulovits, C. Liu, K. Zwejacker, B.W. Reed, T. LaGrange, J.M.K. Wiezorek, G.H. Campbell: In situ transmission electron microscopy of crystal growth-mode transitions during rapid solidification of a hypoeutectic Al-Cu alloy, *Acta Mater.* **65**, 56 (2014)
- 8.36 B.W. Reed, F.R. Chung, M.J. Wang, T. LaGrange, K.J. Koski: Temperature-driven disorder-order transitions in 2D copper-intercalated MoO₃ revealed using dynamic transmission electron microscopy, *2D Materials* **1**, 035001 (2014)
- 8.37 M.K. Santala, S. Raoux, G.H. Campbell: Kinetics of liquid-mediated crystallization of amorphous Ge from multi-frame dynamic TEM, *Appl. Phys. Lett.* **107**, 252106 (2015)
- 8.38 J.T. McKeown, K. Zwejacker, C. Liu, D.R. Coughlin, A.J. Clarke, J.K. Baldwin, J.W. Gibbs, J.D. Roehling, S.D. Imhoff, P.J. Gibbs, D. Tourret, J.M.K. Wiezorek, G.H. Campbell: Time-resolved in situ measurements during rapid alloy solidification: Experimental insight for additive manufacturing, *JOM* **68**, 985 (2016)
- 8.39 O. Bostanjoglo, R. Elschner, Z. Mao, T. Nink, M. Weingartner: Nanosecond electron microscopes, *Ultramicroscopy* **81**, 141 (2000)
- 8.40 O. Bostanjoglo: High-speed electron microscopy, *Adv. Imaging Electron Phys.* **121**, 1 (2002)
- 8.41 H. Dömer, O. Bostanjoglo: High-speed transmission electron microscope, *Rev. Sci. Instrum.* **74**, 4369 (2003)
- 8.42 C.D. Child: Discharge from hot CaO, *Phys. Rev.* **32**, 492 (1911)
- 8.43 O. Bostanjoglo, T. Rosin: Stroboscopic study on ultrasonic activity in electron-microscope, *Mikroskopie* **32**, 190 (1976)
- 8.44 A. Takaoka, K. Ura: Velocity measuring system for interface motion in TEM, *J. Electron Microsc.* **37**, 117 (1988)
- 8.45 H.S. Park, J.S. Baskin, O.-H. Kwon, A.H. Zewail: Atomic-scale imaging in real and energy space developed in ultrafast electron microscopy, *Nano Lett.* **7**, 2545 (2007)
- 8.46 G.V. Spivak, O.P. Pavlyuchenko, V.I. Petrov: Electron microscopic observation of alterations of the do-

- main structure of magnetic films, *Bull. Acad. Sci. USSR Phys. Ser.* **30**, 822 (1966)
- 8.47 O. Bostanjoglo, T. Rosin: Stroboscopic TEM studies of high-frequency magnetic test materials, *Mikroskopie* **36**, 344 (1980)
- 8.48 O.-H. Kwon, B. Barwick, H.S. Park, J.S. Baskin, A.H. Zewail: Nanoscale mechanical drumming visualized by 4D electron microscopy, *Nano Lett.* **8**, 3557 (2008)
- 8.49 D.J. Flannigan, P.C. Samartzis, A. Yurtsever, A.H. Zewail: Nanomechanical motions of cantilevers: Direct imaging in real space and time with 4D electron microscopy, *Nano Lett.* **9**, 875 (2009)
- 8.50 F. Carbone, B. Barwick, O.H. Kwon, H.S. Park, J.S. Baskin, A.H. Zewail: EELS femtosecond resolved in 4D ultrafast electron microscopy, *Chem. Phys. Lett.* **468**, 107 (2009)
- 8.51 B.-L. Qian, H.E. Elsayed-Ali: Electron pulse broadening due to space charge effects in a photoelectron gun for electron diffraction and streak camera systems, *J. Appl. Phys.* **91**, 462 (2002)
- 8.52 D.J. Bradley, A.G. Roddie, W. Sibbett, M.H. Key, M.J. Lamb, C.L.S. Lewis, P. Sachsenmaier: Picosecond x-ray chronoscopy, *Opt. Commun.* **15**, 231–236 (1975)
- 8.53 Z. Chang, A. Rundquist, J. Zhou, M.M. Murnane, H.C. Kapteyn, X. Liu, B. Shan, J. Liu, L. Niu, M. Gong, X. Zhang: Demonstration of a sub-picosecond x-ray streak camera, *Appl. Phys. Lett.* **69**, 133 (1996)
- 8.54 R.K. Li, P. Musumeci: Single-shot MeV transmission electron microscopy with picosecond temporal resolution, *Phys. Rev. Appl.* **2**, 024003 (2014)
- 8.55 D. Xiang, F. Fu, J. Zhang, X. Huang, L. Wang, X. Wang, W. Wan: Accelerator-based single-shot ultrafast transmission electron microscope with picosecond temporal resolution and nanometer spatial resolution, *Nucl. Instrum. Methods Phys. Res. A* **759**, 74 (2014)
- 8.56 S. Hihath, M.K. Santala, K. van Benthem: High-speed nanoscale characterization of dewetting via dynamic transmission electron microscopy, *J. Appl. Phys.* **120**, 085301 (2016)
- 8.57 R.K. Reich, D.D. Rathman, D.M. O'Mara, D.J. Young, A.H. Loomis, E.J. Kohler, R.M. Osgood, R.A. Murphy, M. Rose, R. Berger, S.A. Watson, M.D. Ulibarri, T. Perry, B.B. Kosicki: High-speed, electronically shuttered solid-state imager technology, *Rev. Sci. Instrum.* **74**, 2027 (2003)
- 8.58 T.G. Etoh, D. Poggemann, G. Kreider, H. Mutoh, A.J.P. Theuwissen, A. Ruckelshausen, Y. Kondo, H. Maruno, K. Takubo, H. Soya, K. Takehara, T. Okinaka, Y. Takano: An image sensor which captures 100 consecutive frames at 1000000 frames/s, *IEEE Trans. Electron Dev.* **50**, 144 (2003)
- 8.59 H. Kleine, K. Hiraki, H. Maruyama, T. Hayashida, J. Yonai, K. Kitamura, Y. Kondo, T.G. Etoh: High-speed time-resolved color schlieren visualization of shock wave phenomena, *Shock Waves* **14**, 333 (2005)
- 8.60 M. El-Desouki, M.J. Deen, Q.Y. Fang, L. Liu, F. Tse, D. Armstrong: CMOS image sensors for high speed applications, *Sensors* **9**, 430 (2009)
- 8.61 Y. Tochigi, K. Hanzawa, Y. Kato, R. Kuroda, H. Mutoh, R. Hirose, H. Tominaga, K. Takubo, Y. Kondo, S. Sugawa: A global-shutter CMOS image sensor with readout speed of 1-Tpixel/s burst and 780-Mpixel/s continuous, *IEEE J. Solid-State Circuits* **48**, 329 (2013)
- 8.62 M.D. Grapes, T. LaGrange, L.H. Friedman, B.W. Reed, G.H. Campbell, T.P. Weihs, D.A. Lavan: Combining nanocalorimetry and dynamic transmission electron microscopy for in situ characterization of materials processes under rapid heating and cooling, *Rev. Sci. Instrum.* **85**, 084902 (2014)
- 8.63 M.D. Grapes, Y. Zhang, M.K. Santala, T. Voisin, G.H. Campbell, T.P. Weihs: In situ high-rate mechanical testing in the dynamic transmission electron microscope. In: *MEMS and Nanotechnology*, conference Proceedings of the Society for Experimental Mechanics Series, Vol. 5, ed. by B. Prorok, L. Starman (Springer, Cham 2016)
- 8.64 T. Voisin, M.D. Grapes, Y. Zhang, N.J. Lorenzo, J.P. Ligda, B.E. Schuster, M.K. Santala, T. Li, G.H. Campbell, T.P. Weihs: DTEM in situ mechanical testing: Defect motion at high strain rates. In: *Dynamic Behavior of Materials*, Proceedings of the 2016 Annual Conference on Experimental and Applied Mechanics, Vol. 1, ed. by D. Casem, L. Lamberson, J. Kimberley (Springer, Cham 2016)
- 8.65 W.E. King, G.H. Campbell, A. Frank, B. Reed, J.F. Schmerge, B.J. Siwick, B.C. Stuart, P.M. Weber: Ultrafast electron microscopy in materials science, biology, and chemistry, *J. Appl. Phys.* **97**, 111101 (2005)
- 8.66 H. Rose, R. Spehr: Energy broadening in high-density electron and ion-beams: The Boersch effect. In: *Applied Charged Particle Optics*, *Adv. Electron. Electron Phys. Suppl.* **13C**, ed. by A. Septier (1983) p. 475
- 8.67 G.H. Jansen: *Coulomb Interactions in Particle Beams* (Academic Press, San Diego 1990)
- 8.68 P. Kruit, G.H. Jansen: Space charge and statistical Coulomb effects. In: *Handbook of Charged Particle Optics*, ed. by J. Orloff (CRC, Boca Raton 1997) p. 275
- 8.69 O. Bostanjoglo, F. Heinrich, F. Wunsch: Performance of a laser-pulsed thermal electron gun. In: *Proc. 12th Int. Congr. Electron Microsc.* (1990) p. 124
- 8.70 K.H. Loeffler: Energy-spread generation in electron-optical instruments, *Z. Angew. Phys.* **27**, 145 (1969)
- 8.71 J.M. Cowley: Imaging. In: *High-Resolution Transmission Electron Microscopy and Associated Techniques*, ed. by P. Buseck, J.M. Cowley, L.E. Eyring (Oxford Univ. Press, Oxford 1992)
- 8.72 A. Kulovits, J.M. Wiezorek, T. LaGrange, B.W. Reed, G.H. Campbell: Revealing the transient states of rapid solidification in aluminum thin films using ultrafast *in situ* transmission electron microscopy, *Philos. Mag. Lett.* **91**, 287 (2011)
- 8.73 K. Zwiack, J.T. McKeown, C. Liu, T. LaGrange, B.W. Reed, G.H. Campbell, J.M. Wiezorek: Determination of crystal growth rates during rapid solidification of polycrystalline aluminum by nano-

- scale spatio-temporal *in situ* transmission electron microscopy, *J. Appl. Phys.* **120**, 055106 (2016)
- 8.74 M.M. Winseck, H.-Y. Cheng, G.H. Campbell, M.K. Santala: Crystallization kinetics of the phase change material GeSb₆Te measured with dynamic transmission electron microscopy, *Dalton Trans.* **45**, 9988 (2016)
- 8.75 R.F. Egerton: *Electron Energy Loss Spectroscopy in the Electron Microscope* (Plenum, New York 1986)
- 8.76 R. Henderson: Realizing the potential of electron cryo-microscopy, *Q. Rev. Biophys.* **37**, 3 (2004)
- 8.77 R.F. Egerton: Control of radiation damage in the TEM, *Ultramicroscopy* **127**, 100 (2013)
- 8.78 R. Henderson: Cryoprotection of protein crystals against radiation-damage in electron and x-ray-diffraction, *Proc. Royal Soc. B* **241**, 6–8 (1990)
- 8.79 H.N. Chapman, P. Fromme, A. Barty, T.A. White, R.A. Kirian, A. Aquila, M.S. Hunter, J. Schulz, D.P. DePonte, U. Weierstall, R.B. Doak, F. Maia, A.V. Martin, I. Schlichting, L. Lomb, N. Coppola, R.L. Shoeman, S.W. Epp, R. Hartmann, D. Rolles, A. Rudenko, L. Foucar, N. Kimmel, G. Weidenspointner, P. Holl, M.N. Liang, M. Barthelmess, C. Caleman, S. Boutet, M.J. Bogan, J. Krzywinski, C. Bostedt, S. Bajt, L. Gumprecht, B. Rudek, B. Erk, C. Schmidt, A. Homke, C. Reich, D. Pietschner, L. Struder, G. Hauser, H. Gorke, J. Ullrich, S. Herrmann, G. Schaller, F. Schopper, H. Soltau, K.U. Kuhnle, M. Messerschmidt, J.D. Bozek, S.P. Hau-Riege, M. Frank, C.Y. Hampton, R.G. Sierra, D. Starodub, G.J. Williams, J. Hajdu, N. Timneanu, M.M. Seibert, J. Andreasson, A. Rocker, O. Jonsson, M. Svenda, S. Stern, K. Nass, R. Andritschke, C.D. Schroter, F. Krasniqi, M. Bott, K.E. Schmidt, X.Y. Wang, I. Grotjohann, J.M. Holton, T.R.M. Barends, R. Neutze, S. Marchesini, R. Fromme, S. Schorb, D. Rupp, M. Adolph, T. Gorkhovec, I. Andersson, H. Hirsemann, G. Potdevin, H. Graafsma, B. Nilsson, J.C.H. Spence: Femtosecond x-ray protein nanocrystallography, *Nature* **470**, 73 (2011)
- 8.80 J.C.H. Spence: X-ray imaging: Ultrafast diffract-and-destroy movies, *Nat. Photonics* **2**, 390 (2008)
- 8.81 J. Tenboer, S. Basu, N. Zatsepin, K. Pande, D. Milathianaki, M. Frank, M. Hunter, S. Boutet, G.J. Williams, J.E. Koglin, D. Oberthuer, M. Heymann, C. Kupitz, C. Conrad, J. Coe, G.J. Roy-Chowdhury, U. Weierstall, D. James, D.J. Wang, T. Grant, A. Barty, O. Yefanov, J. Scales, C. Gati, C. Seuring, V. Srajer, R. Henning, P. Schwander, R. Fromme, A. Ourmazd, K. Moffat, J.J. Van Thor, J.C.H. Spence, P. Fromme, H.N. Chapman, M. Schmidt: Time-resolved serial crystallography captures high-resolution intermediates of photoactive yellow protein, *Science* **346**, 1242 (2014)
- 8.82 J.C.H. Spence: Outrunning damage: Electrons vs x-rays—timescales and mechanisms, *Struct. Dyn.* **4**, 044027 (2017)
- 8.83 J.C.H. Spence, G. Subramanian, P. Musumeci: Hollow cone illumination for fast TEM, and outrunning damage with electrons, *J. Phys. B* **48**, 214003 (2015)
- 8.84 S.P. Hau-Riege, R.A. London, H.N. Chapman: *Pulse Requirements for Electron Diffraction Imaging of Single Biological Molecules*, Lawrence Livermore National Laboratory Internal Report UCRL-TR-207533 (Lawrence Livermore National Lab. (LLNL), Livermore 2004)
- 8.85 J.W. Lewellen: Overview of high-brightness electron guns. In: *Proc. 22nd Int. Conf. LINAC* (2004) pp. 842–846
- 8.86 J.R. Fryer: The effect of dose-rate on imaging aromatic organic-crystals, *Ultramicroscopy* **23**, 321 (1987)
- 8.87 D.A. Plemmons, P.K. Suri, D.J. Flannigan: Probing structural and electronic dynamics with ultrafast electron microscopy, *Chem. Mater.* **27**, 3178 (2015)
- 8.88 A. Gahlmann, S.T. Park, A.H. Zewail: Ultrafast electron pulses for diffraction, crystallography and microscopy: Theoretical and experimental resolutions, *Phys. Chem. Chem. Phys.* **10**, 2894 (2008)
- 8.89 L. Piazza, T.T.A. Lummen, E. Quinonez, Y. Murooka, B.W. Reed, B. Barwick, F. Carbone: Simultaneous observation of the quantization and the interference pattern of a plasmonic near-field, *Nat. Commun.* **6**, 6407 (2015)
- 8.90 O. Bostanjoglo, H.P. Gemund: Low-temperature specimen holder for magnetization processes by means of short field pulse, *Mikroskopie* **34**, 188 (1978)
- 8.91 O. Bostanjoglo, T. Rosin: Resonance oscillations of magnetic domain-walls and Bloch lines observed by stroboscopic electron-microscopy, *Phys. Status Solidi (a)* **57**, 561 (1980)
- 8.92 O. Bostanjoglo, R. Liedtke: Tracing fast phase-transitions by electron-microscopy, *Phys. Status Solidi (a)* **60**, 451 (1980)
- 8.93 O. Bostanjoglo, G. Schlotzhauer: Impulse stimulated crystallization of Sb films investigated by time resolved TEM, *Phys. Status Solidi (a)* **68**, 555 (1981)
- 8.94 O. Bostanjoglo, G. Schlotzhauer, S. Schade: Shaping trigger pulses from noisy signals and time-resolved TEM of fast phase-transitions, *Optik* **61**, 91 (1982)
- 8.95 O. Bostanjoglo: Time-resolved TEM of pulsed crystallization of amorphous Si and Ge films, *Phys. Status Solidi (a)* **70**, 473 (1982)
- 8.96 O. Bostanjoglo, G. Hoffmann: Time-resolved TEM of transient effects in pulse annealing of Ge and Ge-Te films, *Phys. Status Solidi (a)* **73**, 95 (1982)
- 8.97 O. Bostanjoglo, W.R. Horinek: Pulsed TEM—A new method to detect transient structures in fast phase-transitions, *Optik* **65**, 361 (1983)
- 8.98 A.A. Ischenko, V.V. Golubkov, V.P. Spiridonov, A.V. Zgurskii, A.S. Akhmanov, M.G. Vabishevich, N. Bagratashvili: A stroboscopic gas-electron diffraction method for the investigation of short-lived molecular-species, *Appl. Phys. B* **32**, 161 (1983)
- 8.99 R.S. Becker, G.S. Higashi, J.A. Golovchenko: Low-energy electron-diffraction during pulsed laser annealing: A time-resolved surface structural study, *Phys. Rev. Lett.* **52**, 307 (1984)
- 8.100 A.P. Rood, J. Milledge: Combined flash-photolysis and gas-phase electron-diffraction studies of

- small molecules, *J. Chem. Soc. Faraday Trans.* **80**, 1145 (1984)
- 8.101 J.D. Ewbank, L. Schäfer, D.W. Paul, O.J. Benson, J.C. Lennox: Real-time data acquisition for gas electron-diffraction, *Rev. Sci. Instrum.* **55**, 1598 (1984)
- 8.102 O. Bostanjoglo, E. Endruschat, F. Heinrich, R.P. Tornow, W. Tornow: Short-interval electron-microscopy and pulsed lasers, *Eur. J. Cell Biol.* **44**, 10 (1987)
- 8.103 O. Bostanjoglo, J. Kornitzky, R.P. Tornow: Nanosecond double-frame electron-microscopy of fast phase-transitions, *J. Phys. E* **22**, 1008 (1989)
- 8.104 O. Bostanjoglo, R.P. Tornow, W. Tornow: Nanosecond-exposure electron-microscopy of laser-induced phase-transformations, *Ultramicroscopy* **21**, 367 (1987)
- 8.105 J.D. Ewbank, J.Y. Luo, J.T. English, R.F. Liu, W.L. Faust, L. Schafer: Time-resolved gas electron-diffraction study of the 193-nm photolysis of 1,2-dichloroethenes, *J. Phys. Chem.* **97**, 8745 (1993)
- 8.106 M. Dantus, S.B. Kim, J.C. Williamson, A.H. Zewail: Ultrafast electron-diffraction. 5. Experimental time resolution and applications, *J. Phys. Chem.* **98**, 2782 (1994)
- 8.107 H. Ihee, V.A. Lobastov, U.M. Gomez, B.M. Goodson, R. Srinivasan, C.Y. Ruan, A.H. Zewail: Direct imaging of transient molecular structures with ultrafast diffractions, *Science* **291**, 458 (2001)
- 8.108 J. Cao, Z. Hao, H.S. Park, C. Tao, D. Kau, L. Blaszczyk: Femtosecond electron diffraction for direct measurement of ultrafast atomic motions, *Appl. Phys. Lett.* **83**, 1044 (2003)
- 8.109 H. Dömer, O. Bostanjoglo: Phase explosion in laser-pulsed metal films, *Appl. Surf. Sci.* **208**, 442 (2003)
- 8.110 B.J. Siwick, J.R. Dwyer, J.E. Jordan, R.J.D. Miller: An atomic-level view of melting using femtosecond electron diffraction, *Science* **302**, 1382 (2003)
- 8.111 O. Bostanjoglo, T. Rosin: Stroboscopic Lorentz TEM at 100 kV up to 100 MHz. In: *Proc. 7th Eur. Congr. Electron Microsc.*, ed. by P. Brederoo, G. Boom (1980) p. 88
- 8.112 O. Bostanjoglo, T. Rosin: Ultrasonically induced magnetoelastic effects observed by stroboscopic electron microscopy. In: *Proc. 6th Eur. Congr. Electron Microsc.*, ed. by D.G. Brandon (1976) p. 360
- 8.113 O. Bostanjoglo, T. Rosin: Ultrasonically induced magnetic reversals observed by stroboscopic electron-microscopy, *Opt. Acta* **24**, 657 (1977)
- 8.114 O. Bostanjoglo, T. Rosin: Mass and relaxation time of domain walls in thin NiFe films from forced oscillations, *J. Magn. Magn. Mater.* **1529**, 15–18 (1980)
- 8.115 O. Bostanjoglo, E. Endruschat: Kinetics of laser-induced crystallization of amorphous germanium films, *Phys. Status Solidi (a)* **91**, 17 (1985)
- 8.116 O. Bostanjoglo, E. Endruschat, W. Tornow: Time-resolved TEM of laser-induced phase transitions in a-Ge and a-Si/Al-films, *Mater. Res. Soc. Symp. Proc.* **71**, 345 (1986)
- 8.117 O. Bostanjoglo, T. Nink: Hydrodynamic instabilities in laser pulse-produced melts of metal films, *J. Appl. Phys.* **79**, 8725 (1996)
- 8.118 O. Bostanjoglo, T. Nink: Liquid motion in laser-pulsed Al, Co, and Au films, *Appl. Surf. Sci.* **109/110**, 101 (1996)
- 8.119 O. Bostanjoglo, J. Kornitzky: Nanoseconds double-frame and streak transmission electron microscopy. In: *Proc. 12th Int. Congr. Electron Microsc.* (1990) p. 180
- 8.120 O. Bostanjoglo, J. Kornitzky, R.P. Tornow: High-speed electron-microscopy of laser-induced vaporization of thin-films, *J. Appl. Phys.* **69**, 2581 (1991)
- 8.121 O. Bostanjoglo, R.P. Tornow, W. Tornow: A pulsed image converter for nanosecond electron-microscopy, *Scanning Microsc. Suppl.* **1**, 197 (1987)
- 8.122 O. Bostanjoglo, R. Niedrig, B. Wedel: Ablation of metal-films by picosecond laser-pulses imaged with high-speed electron-microscopy, *J. Appl. Phys.* **76**, 3045 (1994)
- 8.123 O. Bostanjoglo, F. Heinrich: Producing high-current nanosecond electron pulses with a standard tungsten hairpin gun, *J. Phys. E* **120**, 1491 (1987)
- 8.124 B. Schäfer, O. Bostanjoglo: Laser driven thermionic electron-gun, *Optik* **92**, 9 (1992)
- 8.125 O. Bostanjoglo, D. Otte: High-speed transmission electron-microscopy of laser quenching, *Mater. Sci. Eng. A* **173**, 407 (1993)
- 8.126 O. Bostanjoglo, D. Otte: High-speed electron-microscopy of nanocrystallization in Al-Ni films by nanosecond laser-pulses, *Phys. Status Solidi (a)* **150**, 163 (1995)
- 8.127 T. Nink, F. Galbert, Z.L. Mao, O. Bostanjoglo: Dynamics of laser pulse-induced melts in Ni-P visualized by high-speed transmission electron microscopy, *Appl. Surf. Sci.* **139**, 439 (1999)
- 8.128 T. Nink, Z.L. Mao, O. Bostanjoglo: Melt instability and crystallization in thin amorphous Ni-P films, *Appl. Surf. Sci.* **154**, 140 (2000)
- 8.129 H. Dömer, O. Bostanjoglo: Laser ablation of thin films with very high induced stresses, *J. Appl. Phys.* **91**, 5462 (2002)
- 8.130 H. Dömer, O. Bostanjoglo: Relaxing melt and plasma bubbles in laser-pulsed metals, *J. Appl. Phys.* **94**, 6280 (2003)
- 8.131 T. LaGrange, G.H. Campbell, P.E.A. Turchi, W.E. King: Rapid phase transformation kinetics on a nanoscale: Studies of the $\alpha \rightarrow \beta$ transformation in pure, nanocrystalline Ti using the nanosecond dynamic transmission electron microscope, *Acta Mater.* **55**, 5211 (2007)
- 8.132 J.S. Kim, T. LaGrange, B.W. Reed, R. Knepper, T.P. Weihs, N.D. Browning, G.H. Campbell: Direct characterization of phase transformations and morphologies in moving reaction zones in Al/Ni nanolaminates using dynamic transmission electron microscopy, *Acta Mater.* **59**, 3571 (2011)
- 8.133 T. LaGrange, D.S. Grummon, B.W. Reed, N.D. Browning, W.E. King, G.H. Campbell: Strongly driven crystallization processes in a metallic glass, *Appl. Phys. Lett.* **94**, 184101 (2009)
- 8.134 M.K. Santala, B.W. Reed, S. Raoux, T. Topuria, T. LaGrange, G.H. Campbell: Nanosecond-scale time-

- resolved electron imaging during laser crystallization of GeTe, *Phys. Status Solidi (b)* **249**, 1907 (2012)
- 8.135 M.K. Santala, S. Raoux, T. Topuria, B.W. Reed, T. LaGrange, G.H. Campbell: Distinguishing mechanisms of morphological instabilities in phase change materials during switching, *Thin Solid Films* **571**, 39 (2014)
- 8.136 M.K. Santala, B.W. Reed, T. Topuria, S. Raoux, S. Meister, Y. Cui, T. LaGrange, G.H. Campbell, N.D. Browning: Nanosecond *in situ* transmission electron microscope studies of the reversible Ge₂Sb₂Te₅ crystalline ↔ amorphous phase transformation, *J. Appl. Phys.* **111**, 024309 (2012)
- 8.137 L. Nikolova, T. LaGrange, B.W. Reed, M.J. Stern, N.D. Browning, G.H. Campbell, J.C. Kieffer, B.J. Siwick, F. Rosei: Nanocrystallization of amorphous germanium films observed with nanosecond temporal resolution, *Appl. Phys. Lett.* **97**, 203102 (2010)
- 8.138 L. Nikolova, T. LaGrange, M.J. Stern, J.M. MacLeod, B.W. Reed, H. Ibrahim, G.H. Campbell, F. Rosei, B.J. Siwick: Complex crystallization dynamics in amorphous germanium observed with dynamic transmission electron microscopy, *Phys. Rev. B* **87**, 064105 (2013)
- 8.139 G.C. Egan, K.T. Sullivan, T. LaGrange, B.W. Reed, M.R. Zachariah: *In situ* imaging of ultra-fast loss of nanostructure in nanoparticle aggregates, *J. Appl. Phys.* **115**, 084903 (2014)
- 8.140 J.T. McKeown, N.A. Roberts, J.D. Fowlkes, Y. Wu, T. LaGrange, B.W. Reed, G.H. Campbell, P.D. Rack: Real-time observation of nanosecond liquid-phase assembly of nickel nanoparticles via pulsed-laser heating, *Langmuir* **28**, 17168 (2012)
- 8.141 B. Barwick, D.J. Flannigan, A.H. Zewail: Photon-induced near-field electron microscopy, *Nature* **462**, 902 (2009)
- 8.142 G.C. Egan, T. LaGrange, M.R. Zachariah: Time-resolved nanosecond imaging of nanoscale condensed phase reaction, *J. Phys. Chem. C* **119**, 2792 (2015)
- 8.143 T.T. Li, L.B. Bayu Aji, T.W. Heo, M.K. Santala, S.O. Kucheyev, G.H. Campbell: Effect of medium range order on pulsed laser crystallization of amorphous germanium thin films, *Appl. Phys. Lett.* **108**, 221906 (2016)
- 8.144 R.M. van der Veen, O.-H. Kwon, A. Tissot, A. Hauser, A.H. Zewail: Single-nanoparticle phase transitions visualized by four-dimensional electron microscopy, *Nat. Chem.* **5**, 395 (2013)
- 8.145 D.J. Flannigan, V.A. Lobastov, A.H. Zewail: Controlled nanoscale mechanical phenomena discovered with ultrafast electron microscopy, *Angew. Chem. Int. Ed.* **46**, 9206 (2007)
- 8.146 O.-H. Kwon, V. Ortolan, A.H. Zewail: Macromolecular structural dynamics visualized by pulsed dose control in 4D electron microscopy, *Proc. Natl. Acad. Sci. USA* **108**, 6026 (2011)
- 8.147 A.W.P. Fitzpatrick, S.T. Park, A.H. Zewail: Exceptional rigidity and biomechanics of amyloid revealed by 4D electron microscopy, *Proc. Natl. Acad. Sci. USA* **110**, 10976 (2013)
- 8.148 A.W.P. Fitzpatrick, G.M. Vanacore, A.H. Zewail: Nanomechanics and intermolecular forces of amyloid revealed by four-dimensional electron microscopy, *Proc. Natl. Acad. Sci. USA* **112**, 3380 (2015)
- 8.149 D.J. Flannigan, D.R. Cremons, D.T. Valley: Multimodal visualization of the optomechanical response of silicon cantilevers with ultrafast electron microscopy, *J. Mater. Res.* **32**, 239 (2017)
- 8.150 M.S. Grinolds, V.A. Lobastov, J. Weissenrieder, A.H. Zewail: Four-dimensional ultrafast electron microscopy of phase transitions, *Proc. Natl. Acad. Sci. USA* **103**, 18427 (2006)
- 8.151 V.A. Lobastov, J. Weissenrieder, J. Tang, A.H. Zewail: Ultrafast electron microscopy (UEM): Four-dimensional imaging and diffraction of nanostructures during phase transitions, *Nano Lett.* **7**, 2552 (2007)
- 8.152 O.-H. Kwon, H.S. Park, J.S. Baskin, A.H. Zewail: Nonchaotic nonlinear motion visualized in complex nanostructures by stereographic 4D electron microscopy, *Nano Lett.* **10**, 3190 (2010)
- 8.153 J.S. Baskin, H.S. Park, A.H. Zewail: Nanomusical systems visualized and controlled in 4D electron microscopy, *Nano Lett.* **11**, 2183 (2011)
- 8.154 O.F. Mohammed, P.C. Samartzis, A.H. Zewail: Heating and cooling dynamics of carbon nanotubes by temperature-jump spectroscopy and electron microscopy, *J. Am. Chem. Soc.* **131**, 16010 (2009)
- 8.155 D.J. Flannigan, B. Barwick, A.H. Zewail: Biological imaging with 4D ultrafast electron microscopy, *Proc. Natl. Acad. Sci. USA* **107**, 9933 (2010)
- 8.156 A. Yurtsever, J.S. Baskin, A.H. Zewail: Entangled nanoparticles: Discovery by visualization in 4D electron microscopy, *Nano Lett.* **12**, 5027 (2012)
- 8.157 D.J. Flannigan, A.H. Zewail: Optomechanical and crystallization phenomena visualized with 4D electron microscopy: Interfacial carbon nanotubes on silicon nitride, *Nano Lett.* **10**, 1892 (2010)
- 8.158 U.J. Lorenz, A.H. Zewail: Biomechanics of DNA structures visualized by 4D electron microscopy, *Proc. Natl. Acad. Sci. USA* **110**, 2822 (2013)
- 8.159 J. Hu, G.M. Vanacore, Z. Yang, X. Miao, A.H. Zewail: Transient structures and possible limits of data recording in phase-change materials, *ACS Nano* **9**, 6728 (2015)
- 8.160 B.-K. Yoo, Z. Su, J.M. Thomas, A.H. Zewail: On the dynamical nature of the active center in a single-site photocatalyst visualized by 4D ultrafast electron microscopy, *Proc. Natl. Acad. Sci. USA* **113**, 503 (2016)
- 8.161 D.R. Cremons, D.A. Plemmons, D.J. Flannigan: Femtosecond electron imaging of defect-modulated phonon dynamics, *Nat. Commun.* **7**, 11230 (2016)
- 8.162 D.T. Valley, V.E. Ferry, D.J. Flannigan: Imaging intra- and interparticle acousto-plasmonic vibrational dynamics with ultrafast electron microscopy, *Nano Lett.* **16**, 7302 (2016)
- 8.163 O.-H. Kwon, B. Barwick, H.S. Park, J.S. Baskin, A.H. Zewail: 4D visualization of embryonic, structural crystallization by single-pulse microscopy, *Proc. Natl. Acad. Sci. USA* **105**, 8519 (2008)

- 8.164 H.S. Park, O.-H. Kwon, J.S. Baskin, B. Barwick, A.H. Zewail: Direct observation of martensitic phase-transformation dynamics in iron by 4D single-pulse electron microscopy, *Nano Lett.* **9**, 3953 (2009)
- 8.165 F. Carbone, O.-H. Kwon, A.H. Zewail: Dynamics of chemical bonding mapped by energy-resolved 4D electron microscopy, *Science* **325**, 181 (2009)
- 8.166 R.M. van der Veen, T.J. Penfold, A.H. Zewail: Ultrafast core-loss spectroscopy in four-dimensional electron microscopy, *Struct. Dyn.* **2**, 024302 (2015)
- 8.167 S.T. Park, A.H. Zewail: Photon-induced near-field electron microscopy: Mathematical formulation of the relation between the experimental observables and the optically driven charge density of nanoparticles, *Phys. Rev. A* **89**, 013851 (2014)
- 8.168 H. Liu, J.S. Baskin, A.H. Zewail: Infrared PINEM developed by diffraction in 4D UEM, *Proc. Natl. Acad. Sci. USA* **113**, 2041 (2016)
- 8.169 A. Yurtsever, A.H. Zewail: 4D nanoscale diffraction observed by convergent-beam ultrafast electron microscopy, *Science* **326**, 708 (2009)
- 8.170 A. Yurtsever, A.H. Zewail: Kikuchi ultrafast nanodiffraction in four-dimensional electron microscopy, *Proc. Natl. Acad. Sci. USA* **108**, 3152 (2011)
- 8.171 O.-H. Kwon, A.H. Zewail: 4D electron tomography, *Science* **328**, 1668 (2010)
- 8.172 D.-S. Yang, O.F. Mohammed, A.H. Zewail: Scanning ultrafast electron microscopy, *Proc. Natl. Acad. Sci. USA* **107**, 14993 (2010)
- 8.173 O.F. Mohammed, D.-S. Yang, S.K. Pal, A.H. Zewail: 4D scanning ultrafast electron microscopy: Visualization of materials surface dynamics, *J. Am. Chem. Soc.* **133**, 7708 (2011)
- 8.174 D.-S. Yang, O.F. Mohammed, A.H. Zewail: Environmental scanning ultrafast electron microscopy: Structural dynamics of solvation at interfaces, *Angew. Chem. Int. Ed.* **52**, 2897 (2013)
- 8.175 H.S. Park, J.S. Baskin, A.H. Zewail: 4D Lorentz electron microscopy imaging: Magnetic domain wall nucleation, reversal, and wave velocity, *Nano Lett.* **10**, 3796 (2010)
- 8.176 V. Ortalan, A.H. Zewail: 4D scanning transmission electron microscopy: Single particle imaging and spectroscopy, *J. Am. Chem. Soc.* **133**, 10731 (2011)
- 8.177 A. Yurtsever, R.M. van der Veen, A.H. Zewail: Subparticle ultrafast spectrum imaging in 4D electron microscopy, *Science* **335**, 59 (2012)
- 8.178 A.W.P. Fitzpatrick, U.J. Lorenz, G.M. Vanacore, A.H. Zewail: 4D cryo-electron microscopy of proteins, *J. Am. Chem. Soc.* **135**, 19123 (2013)
- 8.179 L. Sterafini: Micro-bunch production with radio frequency photo-injectors, *IEEE Trans. Plasma Sci.* **24**, 421 (1996)
- 8.180 L.C. Steinhauer, W.D. Kimura: Longitudinal space charge debunching and compensation in high-frequency accelerators, *Phys. Rev. Accel. Beams* **2**, 081301 (1999)
- 8.181 H. Qin, R.C. Davidson: Longitudinal drift compression and pulse shaping for high-intensity particle beams, *Phys. Rev. Accel. Beams* **5**, 034401 (2002)
- 8.182 S.G. Anderson, J.B. Rosenzweig, P. Musumeci, M.C. Thompson: Horizontal phase-space distortions arising from magnetic pulse compression of an intense, relativistic electron beam, *Phys. Rev. Lett.* **91**, 074803 (2003)
- 8.183 D.H. Dowell, J.L. Adamski, T.D. Hayward, P.E. Johnson, C.D. Parazzoli, A.M. Vetter: Results of the Boeing pulse compression and energy recovery, *Nucl. Instrum. Methods Phys. Res. A* **393**, 184 (1997)
- 8.184 F. Zhou, D.B. Cline, W.D. Kimura: Beam dynamics analysis of femtosecond microbunches produced by the staged electron laser acceleration experiment, *Phys. Rev. Accel. Beams* **6**, 054201 (2003)
- 8.185 P. Kung, H.C. Lihn, H. Wiedmann, D. Bocek: Generation and measurement of 50-fs (rms) electron pulses, *Phys. Rev. Lett.* **73**, 967 (1994)
- 8.186 T. Kozawa, T. Kobayashi, T. Ueda, M. Uesaka: Generation of high-current (1kA) subpicosecond electron single pulse, *Nucl. Instrum. Methods Phys. Res. A* **399**, 180 (1997)
- 8.187 M. Reiser: *Theory and Design of Charged Particle Beams* (Wiley, New York 1994)
- 8.188 G. Taban, M.P. Reijnders, B. Fleskens, S.B. van der Greer, O.J. Luiten, E.J.D. Vredendregt: Ultracold electron source for single-shot diffraction studies, *Europhys. Lett.* **91**, 46004 (2010)
- 8.189 B.J. Claessens, S.B. van der Greer, G. Taban, E.J.D. Vredendregt, O.J. Luiten: Ultracold electron source, *Phys. Rev. Lett.* **95**, 164801 (2005)
- 8.190 B.J. Claessens, M.P. Reijnders, G. Taban, O.J. Luiten, E.J.D. Vredendregt: Cold electron and ion beams generated from trapped atoms, *Phys. Plasmas* **14**, 093101 (2007)
- 8.191 M.P. Reijnders, P.A. van Kruisbergen, G. Taban, S.B. van der Greer, P.H.A. Mutsaers, E.J.D. Vredendregt, O.J. Luiten: Low-energy-spread ion bunches from a trapped atomic gas, *Phys. Rev. Lett.* **102**, 034802 (2009)
- 8.192 M.P. Reijnders, N. Debernardi, S.B. van der Greer, P.H.A. Mutsaers, E.J.D. Vredendregt, O.J. Luiten: Phase-space manipulation of ultracold ion bunches with time-dependent field, *Phys. Rev. Lett.* **105**, 034802 (2010)
- 8.193 D.H. Dowell, J.F. Schmerge: Quantum efficiency and thermal emittance of metal photocathodes, *Phys. Rev. Accel. Beams* **12**, 074201 (2009)
- 8.194 N. Debernardi, M.P. Reijnders, W.J. Engelen, T.T.J. Clevis, P.H.A. Mutsaers, O.J. Luiten, E.J.D. Vredendregt: Measurement of the temperature of an ultracold ion source using time-dependent electric field, *J. Appl. Phys.* **110**, 024501 (2011)
- 8.195 A.J. McCulloch, D.V. Sheludko, S.D. Saliba, S.C. Bell, M. Junker, K.A. Nugent, R.E. Scholten: Arbitrarily shaped high-coherence electron bunches from cold atoms, *Nat. Phys.* **7**, 785 (2011)
- 8.196 M.P. Reijnders, N. Debernardi, S.B. van der Greer, P.H.A. Mutsaers, E.J.D. Vredendregt, O.J. Luiten: Time-dependent manipulation of ultracold ion bunches, *J. Appl. Phys.* **109**, 033302 (2011)
- 8.197 E.J.D. Vredendregt, O.J. Luiten: Electron diffraction: Cool beams in great shape, *Nat. Phys.* **7**, 747 (2011)

- 8.198 W.J. Engelen, M.A. van der Heijden, D.J. Bakker, E.J.D. Vredenburg, O.J. Luiten: High-coherence electron bunches produced by femtosecond photoionization, *Nat. Commun.* **4**, 1693 (2013)
- 8.199 L. Cultrera, S. Karkare, H. Lee, X. Liu, I. Bazarov, B. Dunham: Cold electron beams from cryocooled, alkali antimonide photocathodes, *Phys. Rev. Accel. Beams* **18**, 113401 (2015)
- 8.200 R. Akre, D. Dowell, P. Emma, J. Frisch, S. Gilevich, G. Hays, P. Hering, R. Iverson, C. Limborg-Deprey, H. Loos, A. Miahnahri, J. Schmerge, J. Turner, J. Welch, W. White, J. Wu: Commissioning the linac coherent light source injector, *Phys. Rev. Accel. Beams* **11**, 030703 (2008)
- 8.201 A. Chao: *Physics of Collective Beam Instabilities in High Energy Accelerators* (Wiley, New York 1993)
- 8.202 D.A. Edwards, M.J. Syphers: *An Introduction to the Physics of High Energy Accelerators* (Wiley, New York 1993)
- 8.203 J.B. Hastings, F.M. Rudakov, D.H. Dowell, J.F. Schmerge, J.D. Cardoza, J.M. Castro, S.M. Gierman, H. Loos, P.M. Weber: Ultrafast time-resolved electron diffraction with megavolt electron beams, *Appl. Phys. Lett.* **89**, 184109 (2006)
- 8.204 R.K. Li, C.X. Tang, Y.C. Du, W.H. Huang, Q. Du, J.R. Shi, X. Yan, X.J. Wang: Experimental demonstration of high quality MeV ultrafast electron diffraction, *Rev. Sci. Instrum.* **80**, 083303 (2009)
- 8.205 P. Musumeci, J.T. Moody, C.M. Scoby, M.S. Gutierrez, M. Westfall: Laser-induced melting of a single crystal gold sample by time-resolved ultrafast relativistic electron diffraction, *Appl. Phys. Lett.* **97**, 063502 (2010)
- 8.206 Y. Murooka, N. Naruse, S. Sakakihara, M. Ishimaru, J. Yang, K. Tanimura: Transmission-electron diffraction by MeV electron pulses, *Appl. Phys. Lett.* **98**, 251903 (2011)
- 8.207 P.F. Zhu, H. Berger, J. Cao, J. Geck, Y. Hidaka, R. Kraus, S. Pjerov, Y. Shen, R.I. Tobey, Y. Zhu, J.P. Hill, X.J. Wang: Femtosecond time-resolved MeV electron diffraction, *New J. Phys.* **17**, 063004 (2015)
- 8.208 M.Z. Mo, X. Shen, Z. Chen, R.K. Li, M. Dunning, K. Sokolowski-Tinten, Q. Zheng, S.P. Weathersby, A.H. Reid, R. Coffee, I. Makasyuk, S. Edstrom, D. McCormick, K. Jobe, C. Hast, S.H. Glenzer, X. Wang: Single-shot mega-electron volt ultrafast electron diffraction for structure dynamics of warm dense matter, *Rev. Sci. Instrum.* **87**, 11D810 (2016)
- 8.209 R. Li, P. Musumeci: Single-shot ultrafast electron microscopy. In: *25th North Am. Part. Accel. Conf.* (2013)
- 8.210 K. Tanimura: Toward ultrafast electron microscope with femtosecond temporal resolution, atomic-level spatial resolution, and single-shot imaging capability, *Microsc. Microanal.* **21**(Suppl. 3), 651 (2015)
- 8.211 J. Yang, K. Kan, T. Kondoh, Y. Yoshida, J. Urakawa: RF gun based ultrafast electron microscopy. In: *Proc. IPAC2015* (2015), <https://doi.org/10.18429/JACoW-IPAC2015-TUPWI008>
- 8.212 B.W. Reed, S.T. Park, D.J. Masiel: Beyond movie mode: Bridging the gap of time resolution, *Microsc. Microanal.* **22**(Suppl. 3), 706 (2016)
- 8.213 L.F. Allard, S.H. Overbury, W.C. Bigelow, M.B. Katz, D.P. Nackashi, J. Damiano: Novel MEMS-based gas cell/heating specimen holder provides advanced imaging capabilities for *in situ* reaction studies, *Microsc. Microanal.* **18**, 656 (2012)
- 8.214 S. Mehraeen, J.T. McKeown, P.V. Deshmukh, J.E. Evans, P. Abellan, P. Xu, B.W. Reed, M.L. Taheri, P.E. Fischione, N.D. Browning: A (S)TEM gas cell holder with localized laser heating for *in situ* experiments, *Microsc. Microanal.* **19**, 470 (2013)
- 8.215 J.E. Evans, K.L. Jungjohann, N.D. Browning, I. Arslan: Controlled growth of nanoparticles from solution with *in situ* liquid transmission electron microscopy, *Nano Lett.* **11**, 2809 (2011)

Geoffrey Campbell



Materials Science Division
Lawrence Livermore National Laboratory
Livermore, CA, USA
ghcampbell@llnl.gov

Geoffrey Campbell earned his PhD from the University of California, Santa Barbara in 1990. He received an Alexander von Humboldt Foundation scholarship for a postdoctoral appointment at the Max Planck Institute for Metals Research in Stuttgart, Germany. He has worked at Lawrence Livermore National Laboratory for his entire career and is currently the Group Leader for Ultrafast Materials Science.

Joseph McKeown

Materials Science Division
Lawrence Livermore National Laboratory
Livermore, CA, USA
mckeown3@llnl.gov



Joseph McKeown received his PhD from the University of California, Berkeley in 2007. He worked in the Department of Physics at Arizona State University before joining Lawrence Livermore National Laboratory in 2010, where he currently works in the Ultrafast Materials Science Group of the Materials Science Division. His research interests include *in situ* and dynamic transmission electron microscopy.

Melissa Santala

School of Mechanical, Industrial, and
Manufacturing Engineering
Oregon State University
Corvallis, OR, USA
melissa.santala@oregonstate.edu



Melissa Santala received her PhD from the University of California at Berkeley in 2009. She was a Staff Scientist at Lawrence Livermore National Laboratory before joining Oregon State University in Corvallis. Her research involves the application of transmission electron microscopy to study kinetics of phase transformations and the impact of interfaces on the morphological stability of materials.

